buildings

MDPI

Article

Research on the Mechanical Performance of a Mountainous Long-Span Steel Truss Arch Bridge with High and Low Arch Seats

Yao Tan [1,*], Junfeng Shi [1], Peng Liu [2], Jun Tao [3] and Yueyue Zhao [4,5]

[1] Department of Civil Engineering & Architecture and Environment, Hubei University of Technology, Wuhan 430068, China
[2] Hubei Gaolu Highway Engineering Supervision & Consultation Co., Ltd., Wuhan 430051, China; lp2003@yeah.net
[3] China Railway Major Bridge Engineering Group No. 6 Engineering Co., Ltd., Wuhan 430101, China
[4] China Railway Siyuan Survey and Design Group Co., Ltd., Wuhan 430063, China
[5] Hubei Engineering Research Center of Rail Transit Intelligent Bridge Technology, Wuhan 430063, China
* Correspondence: 102110908@hbut.edu.cn

Abstract: The Loushui River Bridge is a mountainous long-span steel truss arch bridge with high and low arch seats. The design and construction of the bridge follow the principle of minimizing environmental damage and promoting sustainable development. In this article, the mechanical performance of this bridge is investigated experimentally and numerically at both the construction and operation stages. A series of validated finite element models were established for linear and nonlinear analyses by introducing geometric imperfections, geometric nonlinearities, and material nonlinearities. Then, several optimized models based on different types of design are compared with the original structure. The results indicate that the stability of the asymmetric bridge met the design requirements in both the construction and operation stages. However, the lateral stability and stiffness of the asymmetric bridge are weak due to the wind hazard that occurred in its mountain ravine. The out-of-plane instability from the short half-arch is the dominant failure mode, and the weakest area is where the arch ribs intersect with the bridge deck. It can be solved by adding more cross bracings without affecting the clearance above the bridge deck or by improving the material intensity of the arch.

Keywords: steel truss arch bridge; design and construction; mountainous area; finite element model; stability; nonlinearity; structural optimization

Citation: Tan, Y.; Shi, J.; Liu, P.; Tao, J.; Zhao, Y. Research on the Mechanical Performance of a Mountainous Long-Span Steel Truss Arch Bridge with High and Low Arch Seats. *Buildings* **2023**, *13*, 3037. https://doi.org/10.3390/buildings13123037

Academic Editor: Giuseppe Santarsiero

Received: 7 November 2023
Revised: 23 November 2023
Accepted: 4 December 2023
Published: 6 December 2023

1. Introduction

As China launches its regional development in mountainous areas, higher demand for bridges that can adapt to mountainous terrain arises. The most representative of these bridges are the Yesanhe Railway Bridge [1] in Hubei province, the Meishikou Bridge in Beijing, the Youshui Railway Bridge [2] in Hunan province, and the Zangmu Yarlung Zangbo Railway Bridge in Tibet. The long-span arch bridge is usually constructed using the cantilever method, and the fastening support system is used for hoisting the arch segments via a cable crane. The lifting tower and fastening tower can be the same or built separately according to specific functions [3–5]. To accommodate the construction site, the arch rib of the Youshui Railway Bridge [6] was directly anchored to the mountains on the two sides of the valley instead of the fastening tower. After the precise match and closure of the arch segments, the Guizhou Yachi River Bridge's [7] arch was cast with concrete using the hanging scaffolding method. The anchorages of the Zigui Changjiang River Highway Bridge [8] were designed as pile–pile cap anchorage and prestressed rock-socketed anchorage.

The mechanical performance of the truss arch bridge is highly related to the axial force of its members. A significant redistribution of the internal forces leads to the damage and failure of the structure [9]. Bonopera et al. proposed two nondestructive static methods for the identification of axial force and verified them via numerical and experimental tests on beams of a small-scale space truss prototype. The result indicated that the accuracy of the tensile and compressive force estimations improves when considering the higher second-order effects induced or measuring the corresponding total displacements precisely [10]. Mases et al. presented a common method for estimating the axial force of structural members that accounts for the rotational inertia and the count of the sensors. The advantage of the method is that little information about the structure is required when five or more sensors assigned to the members are available [11]. For the performance of seismic resistance, Celik and Bruneau investigated two retrofit schemes using buckling-restrained braces (BRBs) as ductile fuses. The method expanded the concept of the deck-truss steel bridge and made it highly applicable to resistant bidirectional earthquake excitation [12]. Wang et al. used a three-span RC box girder bridge as a case study to evaluate the potential benefits of BRBs seismically rehabilitate straight bridges. The addition of BRBs improves the performance of the bridge by decreasing the drifts and reducing the strains [13].

A large quantity of research about actual truss arch bridges has utilized the finite element (FE) method and emphasized the construction and operation [14–24]. Chen et al. investigated the effects of the initial defects, concrete strength, and steel ratio of the arch rib section on the stability of one type of arch bridge based on a certain concrete-filled steel tube (CFST) deck truss arch bridge [25]. Zhang et al. took the Yinchuan South Special Bridge of the Yin-Wu Railway as their research object and focused on analyzing the influences of the lateral strut form, the rise–span ratio, and the non-directional force of the hangers-on stability. The results show that the structural stability of the bridge is most significantly affected by the form of the struts, followed by the effect of the rise–span ratio [26]. Kong et al. analyzed the influence of the local member performance of steel truss arch bridges on the overall stability of the bridges and concluded that the local deformation instability is the primary factor affecting the ultimate bearing capacity of the structure [27]. Wei et al. focused on the wind-resistant safety of the long-span CFST arch bridge during the vertical rotation construction of the stiff-skeleton arch. The installation of wave wind cables can ensure the construction and kinds of parameters that improve the performance, which were also investigated [28].

For the special-shaped spatial arch-rib system, [29–32] the focus has been on the outward-inclined asymmetric steel arch bridge and the establishment of the spatial finite element model to study the mechanical behaviors of the main loadbearing structures including the arch ribs, hangers, and steel box girder. The asymmetric spatial butterfly-shaped steel arch bridge was analyzed in [33,34], which shows that asymmetry does not change the rationality of the bridge structure. Based on the Yingzhou Bridge, Cheng [35] and Ma [36] developed a validated simplified FE model, and then the bridge's stability, ultimate load-carrying capacity, and seismic performance were studied, considering the original design and several modified designs. Kohlmeyer et al. proposed an asymmetrical deck-type CFST arch bridge to evaluate the influence of the general arrangement on its stability. The buckling modes and key factors of the proposed bridge were compared with two other bridges [37]. Gou et al. investigated the dynamic responses of an asymmetrical arch railway bridge subjected to moving trains experimentally and numerically. The results show that the asymmetrical arrangement of the bridge reduces its structural stiffness [38]. In the literature mentioned in the introduction, the construction environment of bridges has mostly been areas with relatively good geological conditions, such as cities and suburbs. However, the construction of the Loushui River Bridge in a ravine environment was far more difficult than that in cities. The structure itself is sophisticated; it is the first large-span double-hinged steel truss arch bridge with high and low arch seats in China. There is still a lack of research on the whole process of the mechanical performance of super-long-span asymmetric steel truss arch bridges in ravine areas.

For this reason, this paper employs the novel asymmetric Loushui River Bridge located in Enshi, China, as its engineering background. The FE model was established using ANSYS and then validated. This investigation simulated the different construction stages on-site and designed several working conditions to study operation stability. The original design was compared with the modified design with various types of struts and two bridges that are the same as the proposed bridge except that they are symmetrically arranged; then, the impact of struts and asymmetry on the stability performance of the arch was concluded respectively.

2. Description of the Loushui River Bridge

2.1. Design of the Loushui River Bridge

The Loushui River Bridge [39–41] spans a 300 m U-shaped ravine with a height difference on both sides of approximately 36 m. To minimize the damage of construction excavation to the environment and ensure the safety, as well as the economy, of the structure, as is shown in Figure 1, the bridge adopts an asymmetrical half-through steel truss arch with a 310 m main span which has two-hinge ends and features two arch seats with different heights. The arch axis complies with an integral catenary, where the virtual calculated span length, rise–span ratio, and axis coefficient of the arch is 340 m, 86.2 m, and 1.7, respectively. The long half-arch spans a 168 m length, and the short half-arch spans a 140 m length. The horizontal distance and the height difference between the starting point of the arch axis of the short half-arch and the theoretical arch axis are 28 m and 36.2 m, respectively. The arch consists of two N lateral truss ribs that are distanced center-to-center at 27 m. Each segment of the arch rib is connected via bolting/welding and is composed of a steel box with a size of 1400 mm × 1600 mm. Wind braces are set between every two segments of the arch rib, and the size of the steel box section of the transverse and diagonal braces is 600 mm × 600 mm. Eighteen hangers and two steel columns with a spacing of 14 m are on one side of the arch rib. The bridge deck is composed of prefabricated slabs and cast-in-place longitudinal and transverse wet joints. The thickness of the asphalt concrete and concrete pavement on the beam is equal to 5 cm and 25 cm. The precast bridge deck is made of C50 concrete, and the wet joint is made of C50 steel fiber concrete. The main components are shown in Figure 2, and all the member sections and material properties are listed in Table 1. The steel arch rib member is composed of a high-strength steel plate that is welded together. The welding quality has an important influence on the stress and performance of the bridge. According to a specification [42], Q460qD and Q345qD steel are determined to be used for bridge construction. The two steels have a low carbon equivalent, which ensures weldability. Meanwhile, the content of the microalloying element is appropriately increased to improve the strength. Q345qD was adopted for the arch chord, cross braces, and steel beam. Q460qD was adopted at the arch feet, as well as the position where the local stress of the hinge shaft is relatively high.

2.2. Construction of the Loushui River Bridge

Due to the complex terrain of the mountainous area, there is no ability to transport enormous bridge segments, and the construction site is not big enough to store a large number of materials. Therefore, the construction method for the bridge is the “hoisting method”, a type of cantilever erection that allows the constructors to manufacture a massive single member in a factory and then carry and fabricate large-scale components at the construction site.

In order to implement the “hoisting method”, the cable hoisting system (CHS) was built, as shown in Figure 3. The CHS consists of three main components: a cable tower, a fastening tower, and steel cables. The construction tower adopts an integrated design of a cable tower and fastening tower; the lower part is the fastening tower, and the upper part is the cable tower, which greatly utilizes space and saves materials at the same time. The steel cables in different locations are divided into three types, depending on their applications: hanging cables, fixing cables, and anchor cables.

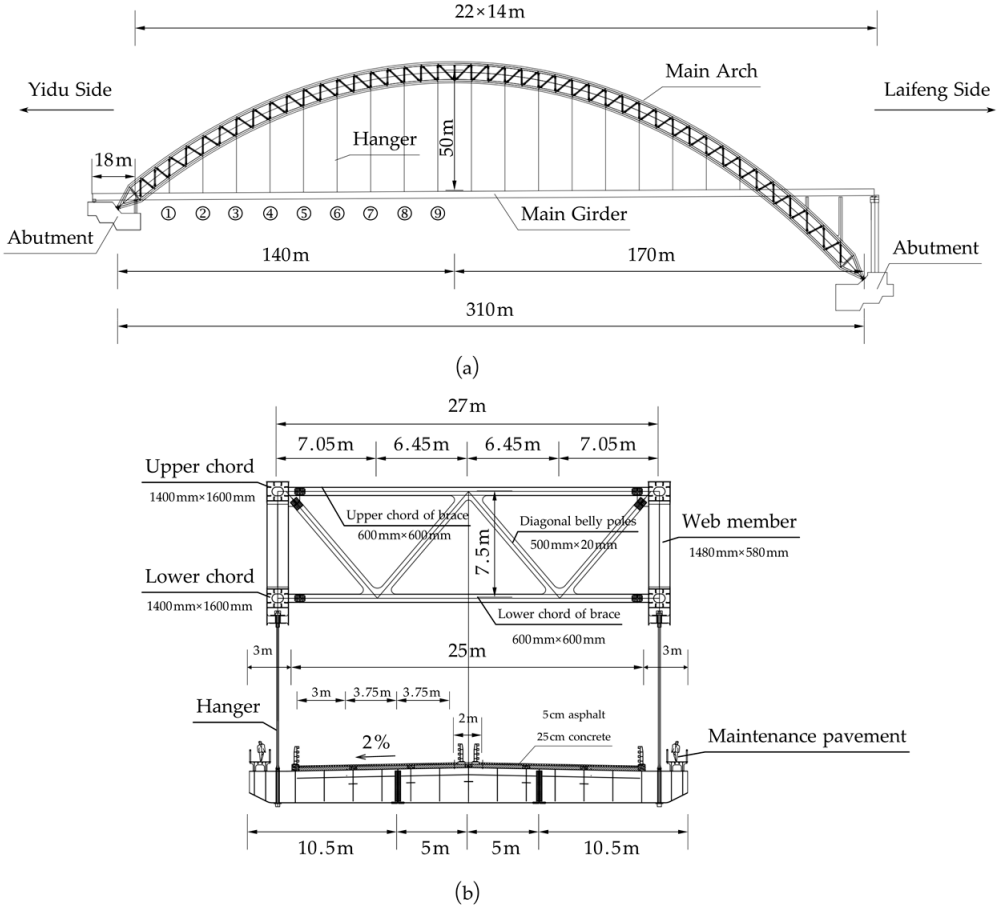

Figure 1. Scheme of the bridge: (**a**) elevation view of the Loushui River Bridge and (**b**) typical cross section of the main arch rib.

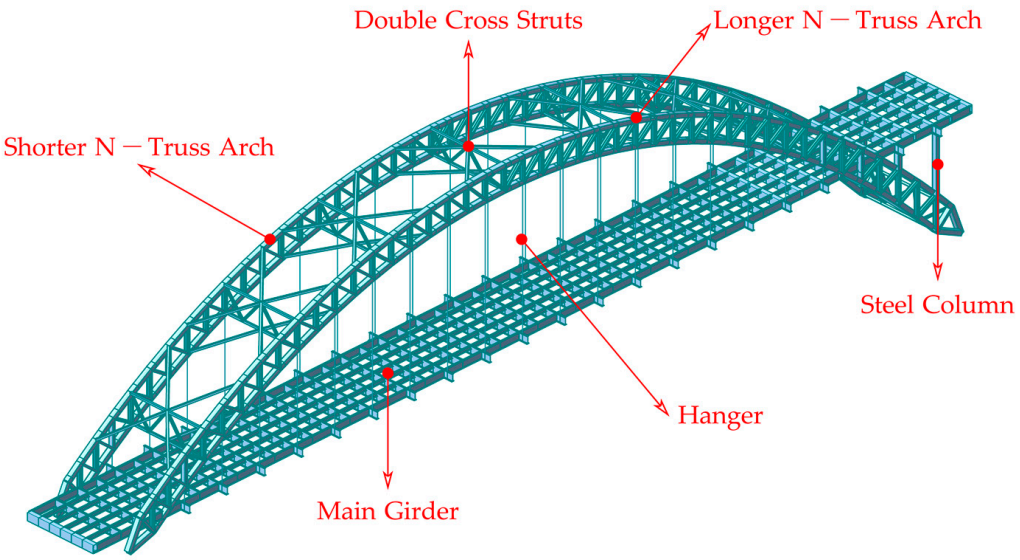

Figure 2. Structural components of the Loushui River Bridge.

Table 1. Cross section and material properties of the main structural components.

Structural Component	Section Type	Area (m^2)	In-Plane Moment of Inertia (m^4)	Out-Plane Moment of Inertia (m^4)	Torsional Moment of Inertia (m^4)
Main arch	Box section	0.28223	0.09695	0.07915	0.11412
Webbing of main arch	I-shaped section	0.09392	0.03056	0.00682	0.01414
Struts	Box section	0.06275	0.00332	0.00299	0.00464
Webbing of main arch	I-shaped section	0.03784	0.00078	0.00212	0.00001
Longitudinal beam	I-shaped section	0.05770	0.03254	0.00115	0.00002
Crossbeam	I-shaped section	0.07363	0.07016	0.00156	0.00003
Steel column	Box section	0.13024	0.04210	0.02917	0.04514
Hanger	Circle section	0.00581	/	/	/
Material	***E*(Mpa)**		**ρ(kN/m^3)**	γ	**σ_y(Mpa)**
Arch steel	2.06×10^5		86.39	0.3	260
Deck steel	2.06×10^5		78.50	0.3	260
Hangers	2.05×10^5		81.84	0.3	1770

E—elastic modulus, γ—Poisson's ratio, σ_y—yield stress of material, and ρ—weight per unit volume of material.

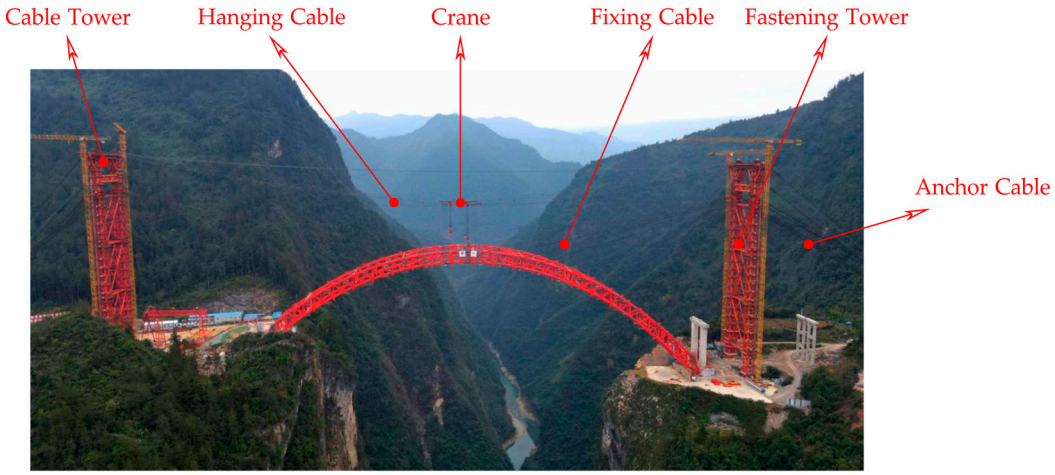

Figure 3. Hoisting installation at the construction site.

The CHS is applied to the whole construction process, which can solve the most complex problems in arch construction well. A flow chart of arch rib construction is shown in Figure 4. Firstly, the arch rib segments that have been assembled and inspected are transported to the lifting platform through a chute, according to the installation sequence. A crane moves along the two sets of hanging cables to the top of the lifting platform and elevates the single arch rib section, which maintains a horizontal state when it is hung. After the crane moves to the target position, the segment is adjusted to the designed inclination angle from the horizontal state while the length of the ropes at both ends of the crane is precisely regulated. When the single segment is installed in place, fixing cables that connect to the anchor cables through the fastening tower are tightened to hold the arch rib in the cantilever state. After a pair of lateral symmetrical segments are installed, the hanging cables are shifted to the centerline of the bridge. Using the same method of lifting and installing wind braces, the installation of a double-width segment is completed. To both sides of the segments, symmetrical suspension is applied to complete the arch ribs together; finally, the fixing cables are dismantled to carry out the bridge deck construction.

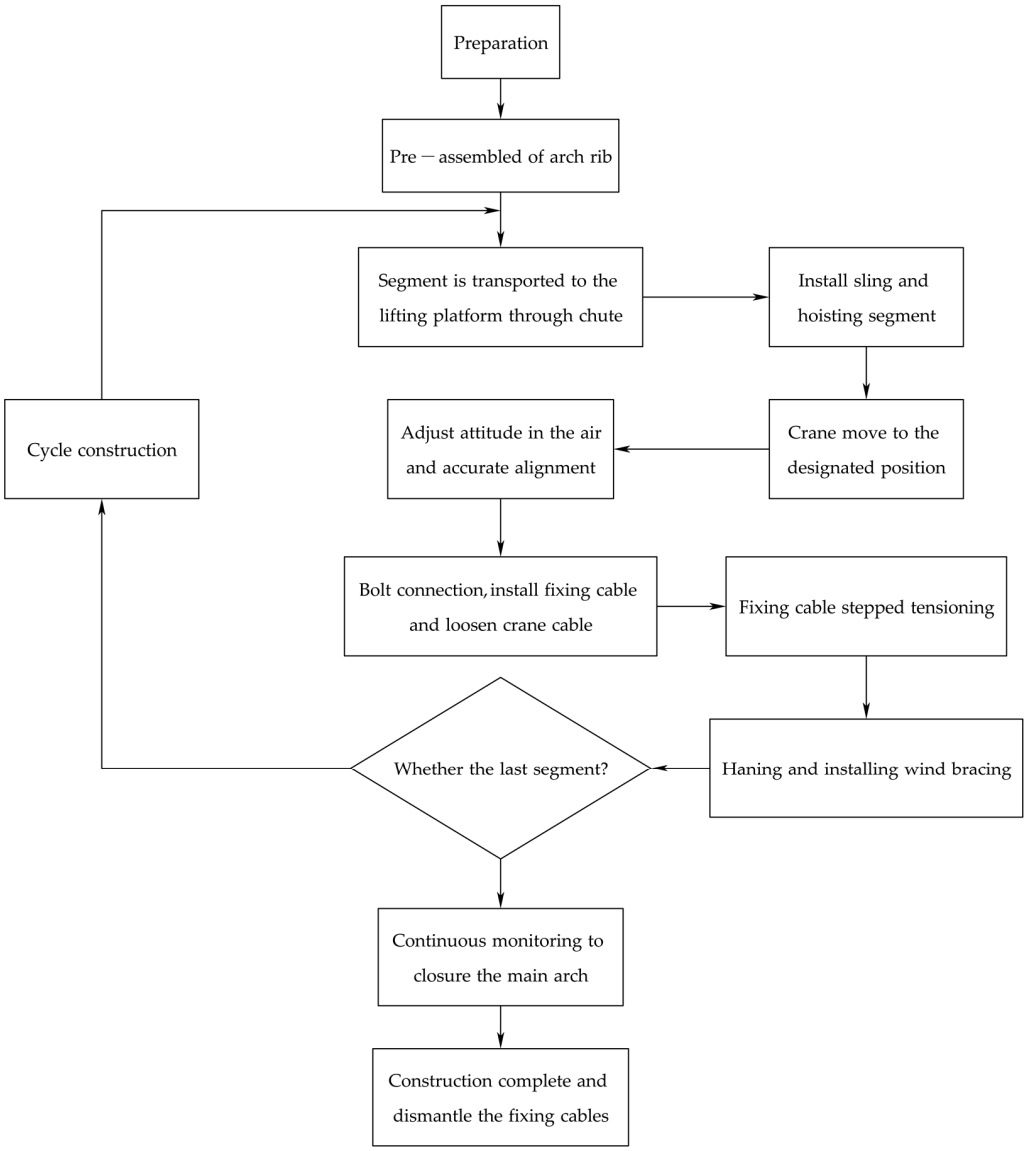

Figure 4. Construction processes of the asymmetrical arch rib.

3. Finite Element Simulations

According to the different working conditions of the Loushui River Bridge, this paper adopts different types of finite element (FE) analysis software to simulate the bridge. Midas Civil 2021 [43,44] was used to simulate the construction stage of the Loushui River Bridge, which was divided into 26 different conditions. The model built with Midas is shown in Figure 5a,b. The upper and lower chords of the arch rib, web members, wind bracing, and build tower were modeled using the beam element. The anchor cable, fixing cable, and hangers were all modeled using the truss element. The bridge deck was simulated using the plate element. Parameters in the model during the construction process, such as the elastic modulus, bulk density, and section shape, were the same as those of the design. A system transition was experienced by the bridge before and after closure. Before the joining of the segment in the vault of the arch, the arch ribs were cantilevered on both sides. The nodes in the arch feet were defined to be articulated, and the bottom of the build towers and the ends of the anchor cable were fixed constraints. After the closure, the main arch ring was formed, and the anchor cable was removed gradually. To minimize the bending moment at the steel beam and hanger joints, the rotation constraint at the element joints was released and finally transformed into a consolidation state. The total mass of the nodal plates and bolts was converted to a uniform load applied to the main chord member when

building the model in response to ensure that the structural deadweight was following the actual situation and to reduce the influence on the analysis. Wind loads were calculated according to a specification [44] and then imposed uniformly on the surface of the arch ribs in the form of static forces. The structural dead load, cable force, secondary permanent load, and vehicle load were carried in the direction of surface forces on the traveling plate and longitudinal beams. The total number of beam elements and truss elements in the FE model of the bridge during the construction stage was 6857 and 124. The total number of beam elements, truss elements, and plate elements in the operation stage was 1667, 36, and 552, respectively.

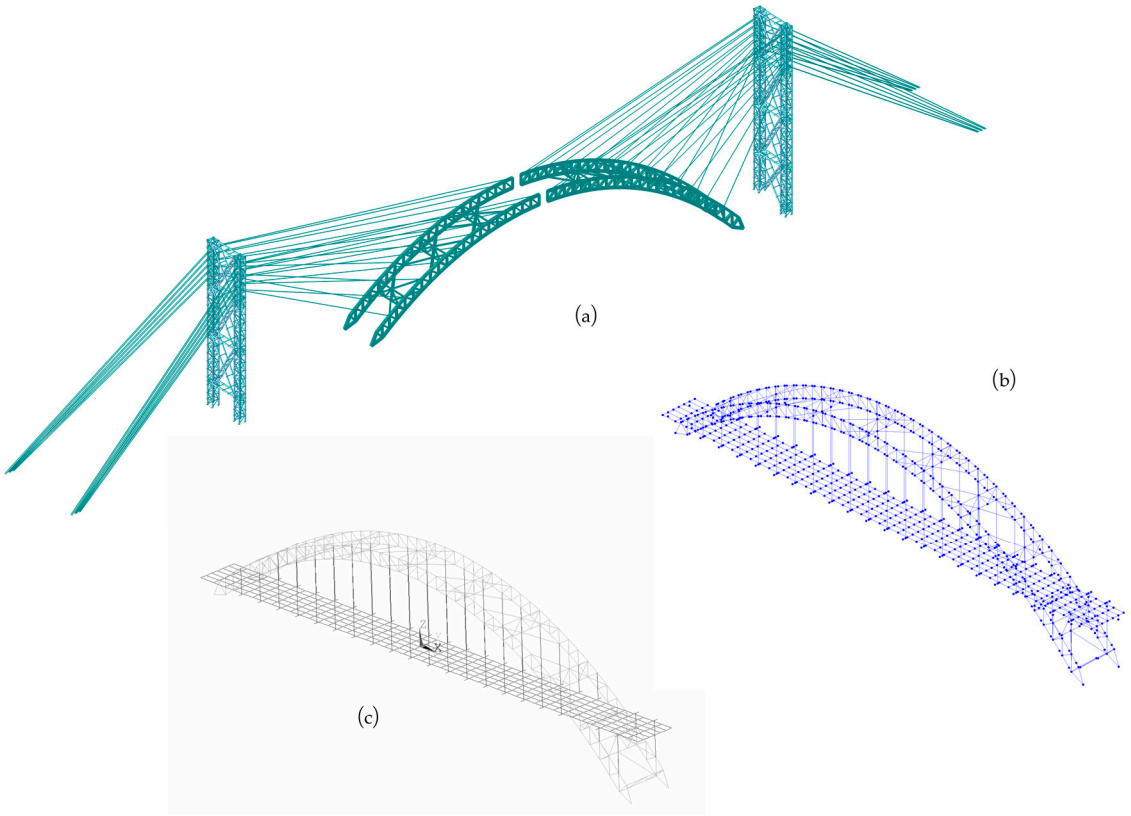

Figure 5. FE model on different platforms and in different stages: (**a**) the Midas model in the construction stage, (**b**) the Midas model in the operation stage, and (**c**) the ANSYS model in the operation stage.

ANSYS 2022 R2 [45] is another tool that was used to calculate the operation stage of the Loushui River Bridge. Considering the modeling complexity and the high computational consumption of the solid elements, this paper utilized the APDL to quickly model the parametric model, as shown in Figure 5c. Firstly, the entire frame of the truss arch was built with nodes; then, elements were grouped according to the different cross sections and the construction order of the truss. Finally, the boundary conditions of the model were simulated based on the practical construction situation. The hanger was LINK180, and the other components were defined as BEAM188. The lane load was distributed on the longitudinal beam of the bridge deck according to the design condition of Midas. The joints of the arch ribs, steel girder, steel column, and hangers were connected using the shared node. The arch foot was hinged, and the two ends of the steel beam were constrained via spherical bearings. The established finite model consisted of 1385 BEAM188 and 36 LINK180 elements. Information on the two types of finite element models is shown in Table 2.

Table 2. Information on the two types of finite element models.

Information	Midas Civil 2021		ANSYS 2022 R2
	Construction	Operation	Operation
Nodes	2858	1713	889
Elements	6981	2259	1421
Mesh size of one beam	Length of every single member		

4. Data Analyses from Field Experiments and Finite Element Simulations

4.1. Numerical Validation of the FE Model

Modal analyses were performed for both the ANSYS model and the Midas model, and the results of Figure 6 show that the modal shapes of the two models were the same for the first three orders but slightly different in the fourth mode and fifth modes. The biggest difference in modal frequency occurred for the fifth order with 4%. The fifth modal shape in Midas was the two main components, the arch rib and the main girder, bending in different degrees. In contrast, the bending direction in the main girder of the ANSYS model was the opposite, and the arch rib had almost no deformation. Therefore, the overall lateral stiffness of the bridge arch rib in the ANSYS model was underestimated. However, the data shown in Table 3 suggest that the model established in ANSYS was qualified since the root-mean-square value (RMS) of all modal frequency relative differences was 2.85% which could be accepted in the numerical simulation aspects.

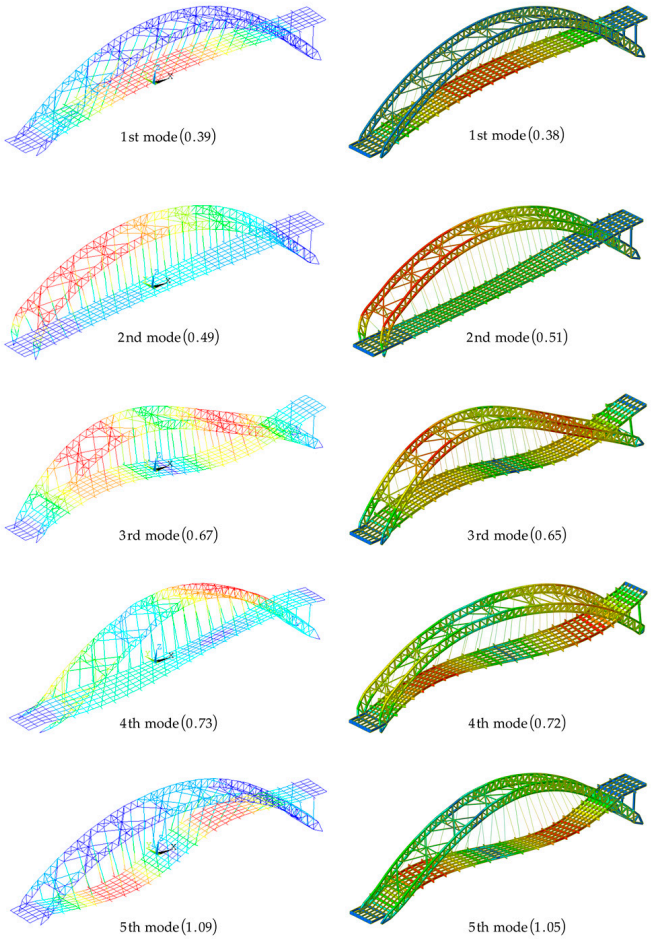

Figure 6. Analytical models for ANSYS (**right**) and MIDAS (**left**).

Table 3. Modal analysis results of the FE model on the Midas platform and ANSYS platform.

FE Model Established in Midas			FE Model Established in ANSYS			
Mode No.	**Modal Frequency (Hz)**	**Mode Shape**	**Mode No.**	**Modal Frequency (Hz)**	**Mode Shape**	**Difference (%)**
1	0.38	Deck's lateral bending in midspan	1	0.39	Deck's lateral bending in midspan	−3.1
2	0.51	Short side arch's lateral bending	2	0.49	Short side arch's lateral bending	2.1
3	0.65	Whole bridge's asymmetry vertical bending	3	0.67	Whole bridge's asymmetrical vertical bending	−3.5
4	0.72	Arch lateral bending from long side with deck's asymmetry lateral bending with slight torsional	4	0.73	Long side arch's lateral bending with deck's torsion	−1.1
5	1.05	Deck's asymmetry lateral bending with arch's slightly lateral bending	5	1.09	Deck's asymmetrical lateral bending	−4.2
6	1.29	Deck laterally bent into three segments	6	1.31	Deck laterally bent into three segments	−1.6
7	1.46	Whole bridge's vertical bending in midspan	7	1.42	Whole bridge's vertical bending in midspan	2.7
8	1.78	Whole bridge's torsion with deck's lateral bending	8	1.73	Whole bridge's torsion	3.1
			RMS			2.9

4.2. Experimental Validation

The quality of the ANSYS model was secondarily validated using the data accessed from the field monitoring of the latest construction conditions of the bridge. The data were compared in two areas: the measured construction line and the internal force in the steel arch segment.

4.2.1. Validating the ANSYS Model Based on Line Control

Line control is an essential part of arch bridge construction. Rigorous monitoring is required throughout the construction process because the errors accumulated along the construction lead the arch alignment away from the design values, resulting in the redistribution of internal forces in the structure. Deformation measurement includes the arch rib elevation measurement and plane coordinate measurement. There were 45 measurement sections in the whole arch, with 44 sections arranged at the front end of each segment and 1 section at the vault. The measurement section of each segment was set 10 cm down from the end of the upper chord, and two measurement points were arranged symmetrically for the section, as shown in Figure 7. The deformation measurement was performed after each segment was installed and the cable was tensioned. Moreover, to prevent the position of the measurement point from movement or destruction, the elevation control reference point was checked every two months. The accuracy of the test was less than 2 mm + 2 ppm. The comparative line shape of the ANSYS model and the line shape obtained from the field measurements are shown in Table 4, where the X, Y, and Z coordinates represent the longitudinal, transverse, and vertical directions of the arch ribs, respectively. Deformation errors of some critical measurement points are listed in Table 4.

Figure 8a,b respectively plot the errors between the numerical simulation and the in situ measurement of the left and right arch ribs of the short half-arch, while Figure 8c,d show the errors of the long half-arch. Before segment YG5, both the left and right sides of the arch rib had an elevation in the Z direction with a maximum value not over 30 mm. This was due to errors in the manufacturing and installation of segmental components, which could only be corrected through the precise regulation of field construction. However, after segment YG5, the upward offset of the arch rib on both sides increased gradually, and the

errors in numerical and field measurements in segment YG10 were truly high, showing that the maximum value of the left side was 68 mm, and the maximum value of the right side was 65 mm. The head-up at the end of the YG10 segment was to ensure that the long half-arch rib could be aligned correctly with the short half-arch, and these errors could be accepted as the line shape control, which does not affect the structure forces. A significant error in the X and Z directions of the long half-arch is illustrated in Figure 8c, which was caused by the cantilever construction of the arch rib and some positional adjustments in installing the segment members.

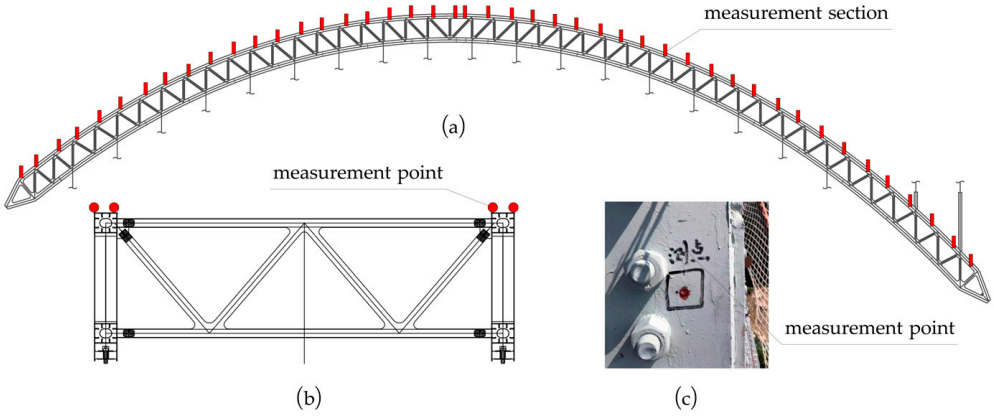

Figure 7. Measurement points of the arch section: (**a**) position of the measuring section, (**b**) arrangement of the measuring point, and (**c**) view of the measuring point.

Table 4. Deformation errors of critical points of the arch rib during construction.

Location			Measured Data (m)			Theoretical Data (m)			Errors (%)		
			X	Y	Z	X	Y	Z	DX	DY	DZ
Yidu side	Left arch	Arch feet	627.638	−14.200	778.138	627.644	−14.2	778.134	−0.001	0	0.0005
			627.650	−12.805	778.137	627.648	−12.8	778.137	0.0003	0.04	0
		YG5	693.594	−14.17	816.314	693.591	−14.2	816.292	0.0004	−0.2	0.003
			693.606	−12.772	816.295	693.59	−12.8	816.292	0.002	−0.2	0.0004
		YG10	764.825	−14.199	828.833	764.811	−14.2	828.765	0.002	−0.007	0.008
	Right arch	Arch feet	627.634	12.784	778.142	627.643	12.8	778.135	−0.001	−0.1	0.0009
			627.618	14.173	778.144	627.638	14.2	778.131	−0.003	−0.2	0.002
		YG5	693.591	14.218	816.328	693.582	14.2	816.305	0.001	0.1	0.003
		YG10	764.818	12.815	828.863	764.798	12.8	828.796	0.003	0.1	0.008
			764.813	14.218	828.86	764.792	14.2	828.796	0.003	0.1	0.008
Laifeng side	Left arch	Arch feet	927.287	−14.213	749.53	927.347	−14.2	749.553	−0.006	0.09	−0.003
			927.3	−12.816	749.522	927.357	−12.8	749.543	−0.006	0.1	−0.003
		LG6	844.327	−14.189	810.377	844.439	−14.2	810.481	−0.01	−0.08	−0.01
		LG12	767.173	−14.185	828.752	767.206	−14.2	828.701	−0.004	−0.1	0.006
			767.178	\	828.758	767.208	−12.8	828.701	−0.004	\	0.007
	Right arch	Arch feet	927.342	14.186	749.557	927.344	14.2	749.556	−0.0002	−0.1	0.0001
			927.352	12.78	749.561	927.344	12.8	749.556	0.0009	−0.2	0.0007
		LG6	844.429	12.793	810.491	844.455	12.8	810.485	−0.003	−0.05	0.0007
			844.429	12.772	810.496	844.447	12.8	810.484	−0.002	−0.2	0.001
		LG12	767.174	12.818	828.769	767.192	12.8	828.709	−0.002	0.1	0.007

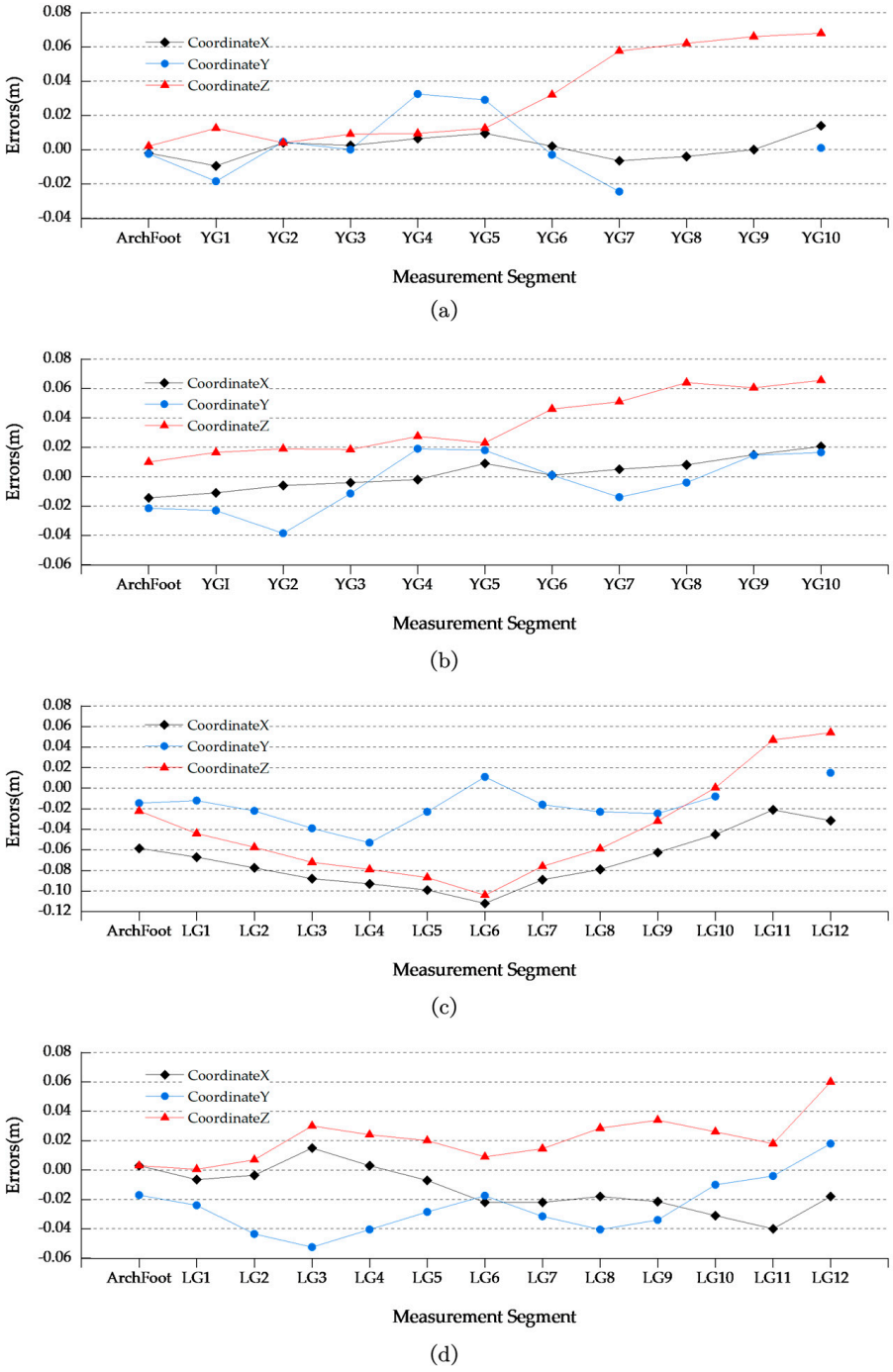

Figure 8. Measured and calculated errors of the arch form: (**a**) the left side of the Yidu arch; (**b**) the right side of the Yidu arch; (**c**) the left side of the Laifeng arch; and (**d**) the right side of the Laifeng arch.

There was some variance numerically and experimentally in the arch bridge, owing to the defaults in the manufacture and installation of components, the complexity of the on-site construction environment, and scheduling during construction. However, the ANSYS model was, overall, close to the measured results for almost all segments.

4.2.2. Validating the ANSYS Model Based on Stress

The stress testing of structures with the strain gauge is used for long-term monitoring after the completion of bridges, and it can be utilized to evaluate the quality of construction.

The bridge was tested by converting the stress value through the stain measurement; the converting equation is defined in Equation (1):

$$\sigma = E \cdot \varepsilon_e \tag{1}$$

However, the realized strain measured, ε, is a total strain, including temperature deformation due to the good thermal conductivity of steel. The total strain can be defined with Equation (2):

$$\varepsilon = \varepsilon_e + \varepsilon_{ns} \tag{2}$$

To avoid the influence of the no-stress strains, the temperature measurement points were placed at the same time as the strain gauge. The ε and no-stress strains ε_{ns} were measured separately, and the elastic strain was determined according to Equation (2).

Eighteen sections on the arch rib were designed as the measurement sections; each section was set up with eight strain gauges, and the detailed layout can be seen in Figure 9. Measurement points 1 to 4 were located in the lower chord section, and 5 to 8 were located in the upper chord section. The bridge used two types of strain sensors installed on the surface of the steel member: manual collection and automatic collection. The manual acquisition method is used to detect the stress of each large segment after installation, and the key sections, such as the arch feet, were equipped with an automatic comprehensive test system to issue an alert on time when an adverse stress occurs. The test accuracy was less than 1 $\mu\varepsilon$.

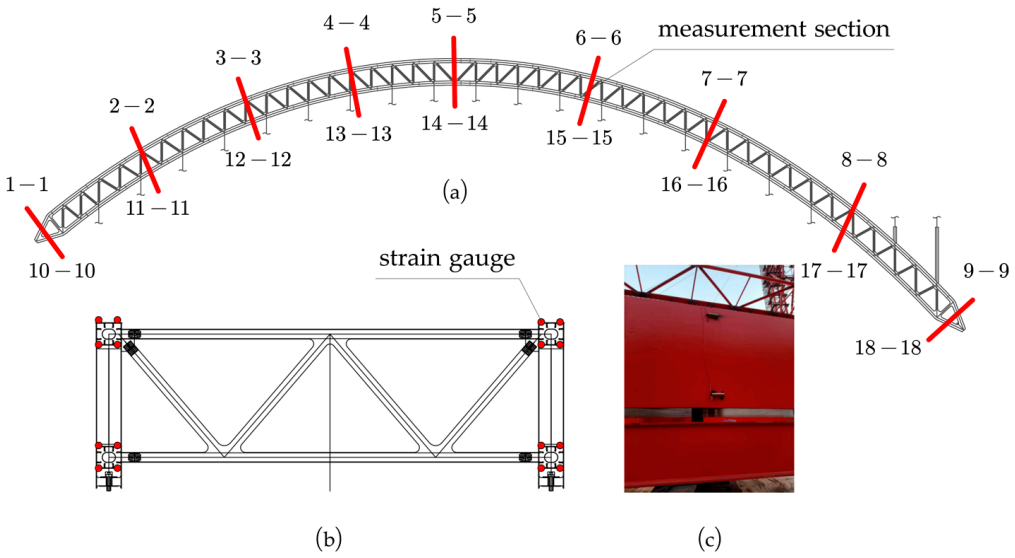

Figure 9. Measurement points of strain: (**a**) position of the measuring section, (**b**) arrangement of the measuring point, and (**c**) view of the measuring point.

The stress errors of the arch feet during construction are shown in Table 5. Two regularities can be summarized from the comparative results of measurement and simulation shown in Figure 10. The strains acquired at the lower chord were generally greater than those at the upper chord, showing from the chart that the stress value decreased from points 1 to 8. The short half-arch described in Section 4.4 showed an opposite pattern, presumably due to the no-stress strains caused by construction loads. The strain in the arch foot section was greater than the strain in the midspan section. Although the design of two hinges with high and low arch abutments solved the problems of an uneven temperature difference and sedimentation, the arch feet were extremely unfavorable under multiple loads, which led to generally high stress in the foot of the arch cross section.

Table 5. Stress errors of the arch feet during construction.

Working Condition	Location	Measurement Point	Measured Data (m)	Theoretical Data (m)	Errors (m)	Errors (%)
Finish cable tensioning of YG10 segment	Yidu side	1-1	1	−27.76	−30.1	2.34	−8.4
			2	−30.46	−28.2	−2.26	7.4
			3	−30.31	−28.3	−2.01	6.6
			4	−24.97	−27.9	2.93	−11.7
			5	−24.75	−22.6	−2.15	8.7
			6	−22.38	−24	1.62	−7.2
			7	−24.22	−26.3	2.08	−8.6
			8	\	\	\	\
		10-10	1	−31.43	−28.6	−2.83	9.0
			2	−30.7	−29.2	−1.5	4.9
			3	−25.39	−27.2	1.81	−7.1
			4	−25.95	−28.5	2.55	−9.8
			5	−25.64	−24	−1.64	6.4
			6	−20.46	−22.9	2.44	−11.9
			7	\	\	\	\
			8	−24.11	−26.1	1.99	−8.3
Finish cable tensioning of LG12 segment	Laifeng side	9-9	1	−28.47	−30.4	1.93	−6.8
			2	−30.54	−28.2	−2.34	7.7
			3	−27.4	−29.2	1.8	−6.6
			4	−28.45	−26.7	−1.75	6.2
			5	−20.44	−22.9	2.46	−12.0
			6	−22.61	−24.7	2.09	−9.2
		18-18	1	−26.22	−28.1	1.88	−7.2
			2	−28.12	−30.8	2.68	−9.5
			3	−25.04	−26.8	1.76	−7.0
			4	−26.58	−29.4	2.82	−10.6
			5	−23.01	−25.1	2.09	−9.1
			6	−19.85	−22.2	2.35	−11.8

It is difficult to match the measurement stresses of the long-span arch bridge with the simulation perfectly because of the non-homogeneous nature of the material, which is influenced by many factors, such as design parameters and construction conditions. However, the ANSYS model's stress and the measurement stress were the same in variation, with the maximum difference not bigger than 3 Mpa. At this point, a validated computational FE model was obtained for the following studies.

4.3. Stability Analysis under a Wind Load

4.3.1. Buckling Analysis in the Construction Stage

Before the closure of the arch rib, the structure relied on the fixing cable and arch foot support to maintain its balance in the vertical direction, and the lateral stability of the bridge was ensured via wind braces and windproof cables. The structure is complex, and the stability requirements are very high. Stability analysis was carried out for this construction stage, and the working conditions were adopted as in the case of dead load and wind load, respectively, as we can see in Table 6.

The stability eigenvalue varied with the progress of the construction. Taking the third construction condition as the boundary, the stability eigenvalue showed a pattern of increasing and then decreasing. At the maximum cantilever state, which was the 12th construction condition, the stability eigenvalue reached its minimum. After the completion of the closure, the steel truss structural system was formed, and the stability was significantly improved.

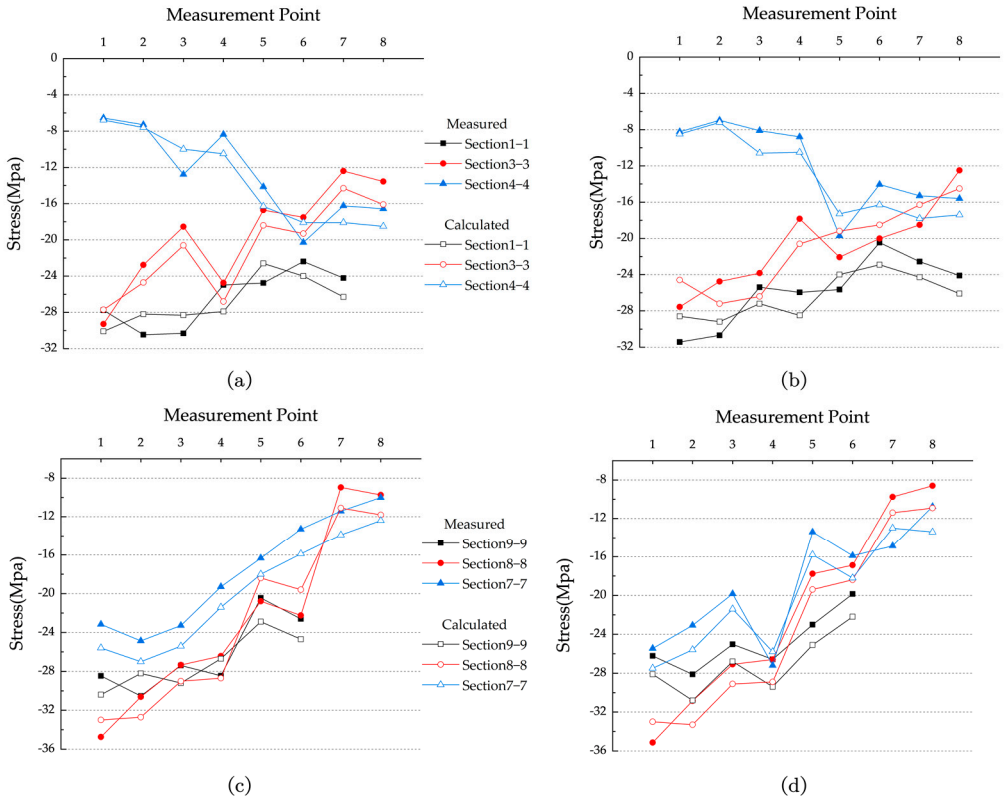

Figure 10. Measured and calculated errors of arch stress: (**a**) the left side of the Yidu arch; (**b**) the right side of the Yidu arch; (**c**) the left side of the Laifeng arch; (**d**) the right side of the Laifeng arch.

Table 6. Lowest-order stability eigenvalue for the construction stage.

Construction Condition	Dead Load		Wind Load		Variation %
	Stability Eigenvalue	Buckling Shape	Stability Eigenvalue	Buckling Shape	
LG1	26.33	Out-of-plane instability	26.33		0
LG2	31.45		31.45		0
LG3 and YG1	34.81		34.81		0
LG4 and YG2	34.70	In-plane instability	27.45		−20.893
LG5 and YG3	27.81		19.43		−30.133
LG6 and YG4	27.03		20.78		−23.122
LG7 and YG5	28.51		15.18	Out-of-plane instability	−46.756
LG8 and YG6	23.71		11.29		−52.383
LG9 and YG7	20.34	Out-of-plane instability	14.01		−31.121
LG10 and YG8	19.12		11.67		−38.964
LG11 and YG9	19.01		11.34		−40.347
LG12 and YG10	18.88		11.15		−40.943
Arch closure	19.98		12.27		−38.589
Wind bracing for closure	22.43		13.84		−38.297
Dismantle fixing cable	22.17		12.46		−43.798

The trend in the stability of the structure was the same for both loading conditions. However, the stability eigenvalue of the structure under transverse wind was generally lower, with a maximum difference of more than 50%. This indicates that the arch rib construction stage was greatly affected by the cross-bridge wind load, which should be emphasized in windy weather.

4.3.2. Buckling Analysis in the Operation Stage

The moving load tracker of Midas Civil was utilized to search for the operation conditions with the maximum deflection, maximum axial force, and maximum bending moment of the arch rib under different vehicle loads as the most unfavorable loading arrangement. The nine most adverse moving load conditions, which can be classified into three categories, were determined through two kinds of loading methods: one-lane bias loading and two-lane bias loading. The three kinds of load combinations are a full-lane load, a right-lane load, and a left-lane load, respectively.

Both steel segment fabrication and erection errors can lead to deviations in structure construction. Therefore, the nodal displacements of the linear elastic stabilized first-order buckling mode were taken as the initial defects of the structure applied to each node of the bridge. According to a specification, this paper took L/300, L/600, and L/900 (L is the calculated span diameter of the bridge) as the factors to impose defects on the calculated model and analyze the influence of the corresponding geometrical initial offset on the stability performance of the bridge. The model with no imperfection was also taken as a comparison, and the first-order stability eigenvalue obtained from the linear elastic analysis for each working condition and defect case is shown in Table 7.

Table 7. Lowest-order stability eigenvalue for ten load cases.

Case No.	Combination	First Order				Sixth Order
		No Defects	L/900	L/600	L/300	No Defects
1	Dead load	6.926	/	/	/	31.938
2	Dead load + wind load + full-lane load with the greatest displacement	6.326	6147	6.141	6.140	27.774
3	Dead load + wind load + full-lane load with the greatest stress	6.165	5.993	5.983	5.979	28.648
4	Dead load + wind load + full-lane load with the greatest moment	6.061	5.885	5.881	5.890	27.748
5	Dead load + wind load + right-lane load with the greatest displacement	6.373	6.192	6.186	6.184	28.310
6	Dead load + wind load + right-lane load with the greatest stress	6.265	6.084	6.077	6.075	28.890
7	Dead load + wind load + right-lane load with the greatest moment	6.288	6.111	6.105	6.104	27.892
8	Dead load + wind load + left-lane load with the greatest displacement	6.359	6.177	6.172	6.170	28.264
9	Dead load + wind load + left-lane load with the greatest stress	6.251	6.066	6.063	6.063	28.900
10	Dead load + wind load + left-lane load with the greatest moment	6.196	6.012	6.010	6.009	28.681
Instability shape		Out-plane antisymmetric				In-plane anti-symmetric

Comparing the three load combinations revealed that the structural stability was the worst with the full-lane load, followed by the left-lane load, while the right-lane load had the largest stability coefficient. The data obtained for the three load conditions for each load combination also conformed to a certain pattern, showing that the case with the largest bending moment of the arch rib had the lowest stability coefficient, followed by the case with the largest axial force and with the largest deflection of the vault in the arch rib, for which the stability eigenvalue increased incrementally. The structure had the lowest load-carrying capacity under the operating condition of Case 4, with a stability eigenvalue of 6.061, while the next highest had a stability eigenvalue of 6.165 in Case 3. The arch ribs of the bridge were mainly subjected to pressure and had poor bending resistance, which seriously affected the stability of the bridge in the case with the largest bending moment.

The effects of vault displacement on the structure were relatively small. Structural asymmetry on both sides of the vault was reflected in asymmetric structural deformation under live loads, which also led to location differences with the maximum deflection of

the arch and the center of the deck. This situation reduced the effect of displacement on structural stability. It can be concluded from the description above that the arrangement of the live load affected the stability of the asymmetrical structure slightly, and the influence of the structure's constant load on the overall stability was significant. The average stability coefficient of the overall structure of the bridge under various working conditions was above, which met the load-carrying capacity requirements for structural linear elastic stability.

The stability eigenvalue of the structure under all operating conditions was reduced when considering the imperfections caused by the manufacturing and installation. Among all the cases, the defects from L/900 to L/300, the stability eigenvalue of Case 5 was reduced from 6.265 to 6.075, with a total reduction of 3.031%, which was the largest reduction of the cases, and the least stable case, Case 4, had a stability eigenvalue that decreased from 6.061 to 5.8798, a reduction of 2.985%. The linear elastic stability analysis during the operational stage of the structure illustrated that the initial geometrical defects had a limited effect on the stability of the structure, with the maximum rate of decrease in stability not exceeding 5%.

4.3.3. Stability Considering Geometric Nonlinearity

The load–displacement curves for geometrically nonlinear stabilization at each defect scale are illustrated in Figure 11. Taking the case of a defect ratio of L/300 as an example, the change of the load–displacement curve under geometric nonlinearity could be divided into three periods. In the elastic phase, the slope of the load–displacement curve was great. The deformation rate of the whole structure with the growth of the load was low, and the material of the structure was far from reaching plasticity. In the second stage, the slope of the load–displacement curve became less and appeared as a smooth transition section on the image, which represents the acceleration of the deformation rate of the structure. The material in some areas of the steel truss arch bridge reached yielding, and the corresponding areas show elastic–plastic deformation. The other members of the structure would also enter the elastic–plastic stage with the expansion of the plastic region. When the displacement of the arch top reached 600 mm, the slope of the curve started to decrease sharply until it tended to zero, and the structure eventually lost its carrying capacity due to the excessive deformation of the steel arch ribs, which is the destructive stage of the structure. Since the deflection of the vault remained in a relatively small range until the destructive stage, it could be seen that the vault was not the starting point of the diffusion of the plastic deformation of the structure. By analyzing the finite element loading step, it could be observed that the starting point of yielding for the Loushui River Bridge is at the node of the short half-arch steel arch rib, which has less of a wind bracing arrangement compared to the long half-arch side, and at the same time, the yielding displacement is oriented laterally, so the destruction of the steel truss arch rib is a localized failure of the arch rib node.

The load–displacement curves with initial defect ratios of L/900 and L/600 were less distinguishable, suggesting that the effect on structural stability was also relatively less in the case of smaller initial defect ratios. However, the differences in the load–displacement curves started to be significant as the proportion of initial defects increased. This difference manifested in the fact that the greater the proportion of defects, the lower the total structural load-carrying capacity, while the extension of the vault deflection grew.

The nonlinear stability coefficients for the geometrical nonlinearity of the structure for each defect ratio are illustrated in Table 8. The geometric nonlinear analysis without considering the geometric initial defects resulted in a structural stability coefficient of 5.0589, which was reduced by 16.53%, concerning the elastic analysis. The reduction rate was less than 20%, and the impact of geometric nonlinearity on structural stability was weak. The stability coefficients were 4.8051, 4.7023, and 4.3941 for the three cases with defect ratios ranging from L/900 to L/300, which followed the trend of the larger the defects, the lower the load-carrying capacity. The stability coefficient was diminished by 27.498%, concerning the linear elasticity analysis, for a defect ratio of L/300, which was a

reduction rate of nearly 30%; hence, the initial defects made a considerable contribution to the reduction of the geometric nonlinear stability of the structure.

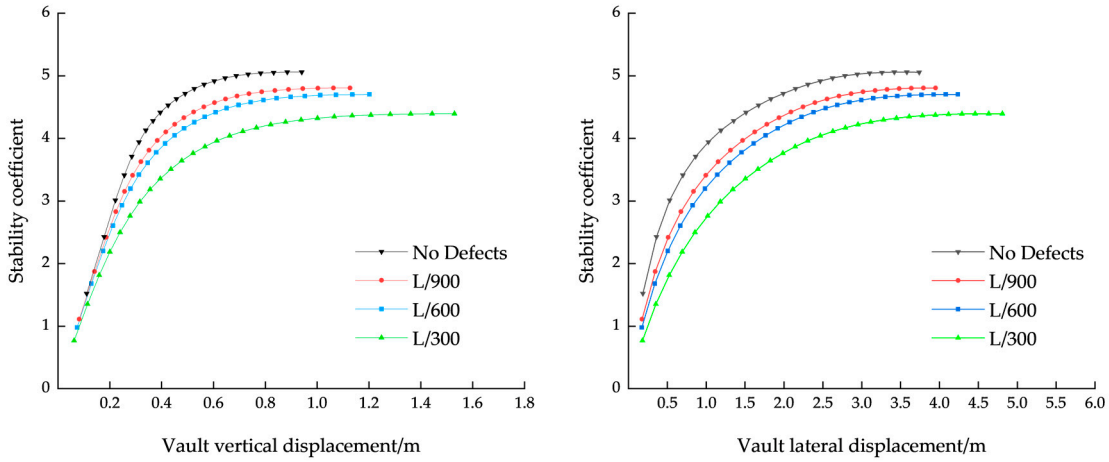

Figure 11. Load–displacement curves for geometric nonlinearity in different defects: (**a**) vertical displacement and (**b**) lateral displacement.

Table 8. Ultimate load multiple for geometric nonlinearity in different defects.

Defects	Nonlinear Stability Coefficient	Reduction Rate/%
0	5.0589	
L/900	4.8051	5.016
L/600	4.7023	7.049
L/300	4.3941	13.140

4.3.4. Stability under Material Nonlinearity

In the dual nonlinear stability analysis of the Loushui River Bridge, the initial defect imposition method during the analysis was the same as during the geometric nonlinear stability analysis, and the defect ratios were still selected as 0~L/300. The load–displacement curves under different defect ratios are shown in Figure 12.

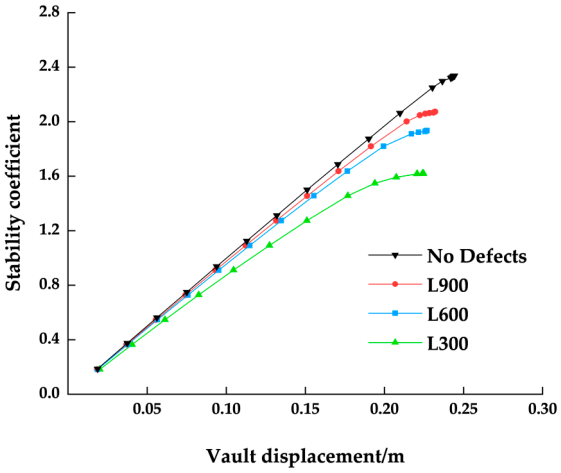

Figure 12. Load–displacement curves for double nonlinearity with different defects.

The stability coefficient of the structure decreased significantly after considering geometric nonlinearity combined with material nonlinearity. The structural stability coefficient

without initial defects was 2.338, which was 61.425% and 53.786% lower than the coefficients for linear elasticity analysis and geometric nonlinearities only, respectively. Therefore, the results of stability calculations that did not take into account material nonlinearity were too conservative and varied greatly from the real results. In the design of a steel truss arch bridge, material nonlinearity should be included in the stability analysis of the bridge.

The contrast between the stability of the structure with different defects is shown in Table 9. The percentage of the defects increased, and the rate of decrease in the stability coefficients when considering only geometric nonlinearities was 5.016%, 7.049%, and 13.140%, respectively, while the rate of decrease in the stability coefficients when considering dual nonlinearities was 11.352%, 17.229%, and 30.724%, respectively. The reduction in structural stability was significant after considering the material nonlinearity, which indicates that material nonlinearity amplifies the effect of the initial defects; especially when the initial defect ratio was L/300, the stability coefficient reduction rate was much larger than other working conditions, reaching 30%.

Table 9. Ultimate load for double nonlinearity with different defects.

Defects	Nonlinear Stability Coefficient	Variation/%
0	2.3379	
L/900	2.0725	11.352
L/600	1.9351	17.229
L/300	1.6196	30.724

4.4. Effects of Asymmetry

To study the influence of asymmetry on the stability of the Loushui River Bridge, two other finite element models with the same span of 310 m were established. Model I was an original design model of the Loushui River Bridge. Model II was a through steel truss arch bridge with an equal height arch seat and span of 310 m, which needed to be excavated from the mountain of the Yidu side. Model III was a through steel truss arch bridge with an equal height arch seat and span of 310 m, for which a landfill of the mountain of the Laifeng side was needed.

The results of the calculations are shown in Table 10 and Figure 13, which indicate that symmetry affects the stability of the structure significantly. The stability coefficients of Model II under buckling and geometric nonlinearity were 14.1240 and 13.2805, respectively, which were 119.225% and 136.839% higher than those of Model I. The stability coefficients of Model III were 5.7057 and 5.4660, which were 11.439% and 2.522% lower compared to the stability coefficients of Model I, respectively.

Table 10. Stability analysis results for different models.

Models	Buckling Analysis		Nonlinear Analysis	
	Lowest Stability Eigenvalue	Variation/%	Stability Coefficient	Variation/%
I	6.442		5.607	
II	14.124	119.225	13.281	136.84
III	5.706	−11.439	5.466	−2.52

In the elastic phase, the ultimate load-carrying capacity of the asymmetric arch bridge of Model I was greater than that of the remaining two models. During the elastic–plastic stage, both Models I and III had a high deformation capacity, while the vault displacement of Model II could not continue to increase, and the structure quickly lost its carrying capacity. Overall, the deformation capacity of symmetrical arch bridges is greater than that of asymmetrical arch bridges.

The excavation of the arch seat when building Model II was huge, and the construction site was located in a cliff position, which entails high risk and has a huge impact on

environmental damage. The construction of Model III faced the same sustainability issues as Model II while being less stable than the original design. Therefore, the original design can be concluded to be the most reasonable, both economically and environmentally.

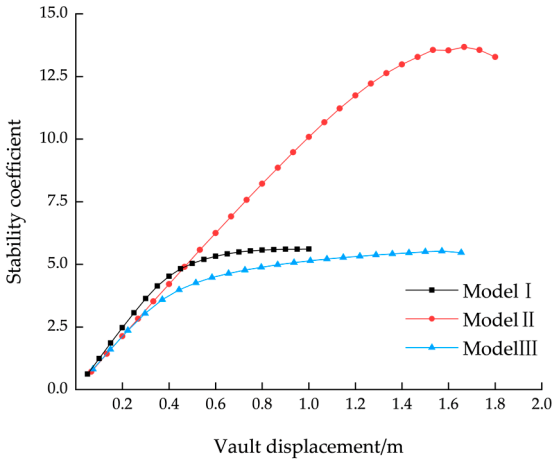

Figure 13. Load–displacement curves for different asymmetry.

4.5. Components

4.5.1. Main Components Affect Stability

To investigate the effect of the nonlinearities of different members in a bridge on the overall stability, four different member nonlinearization schemes were designed. Case 1 considered the material constitutive relations for steel arch ribs, steel girders, and steel hangers as ideally elastic–plastic. Case 2 considered only steel arch ribs as ideally elastic–plastic. Case 3 considered only the bridge steel girders as ideally elastic–plastic. Case 4 considers only the steel hangers as ideally elastic–plastic.

The structural stability coefficients under each case are shown in Table 11, and the difference between the stability coefficients of Case 1 and Case 2 was only 2.169%, which indicates that the material properties of the steel girders and steel hangers affect the overall stability of the bridge quite slightly. The difference among the stabilization coefficients of Case 1 compared to Case 3 and Case 4 was more than 80%. Therefore, the material properties of steel arch ribs have the greatest influence on the overall structural stability, and the safety of steel arch ribs represents the overall safety of the bridge. The overall stability of the structure can be improved by increasing the steel strength of the steel arch ribs so that they enter the plastic state much later.

Table 11. Ultimate loads for different component materials.

Case No.	Nonlinear Stability Coefficient	Variation/%
1	2.2769	
2	2.3269	2.196
3	4.1171	80.820
4	4.1492	82.230

Figure 14 reveals the destabilization process for the four cases. For conditions III and IV, the steel arch ribs were made of elastic–plastic material, the deflection values tolerated by the arch before the bridge was destabilized were very small, and the steel girders of the bridge deck were still in the elastic deformation stage when the plastic damage of the arch ribs occurred. The plastic failure of the arch ribs contributed to the overall destruction of the structure.

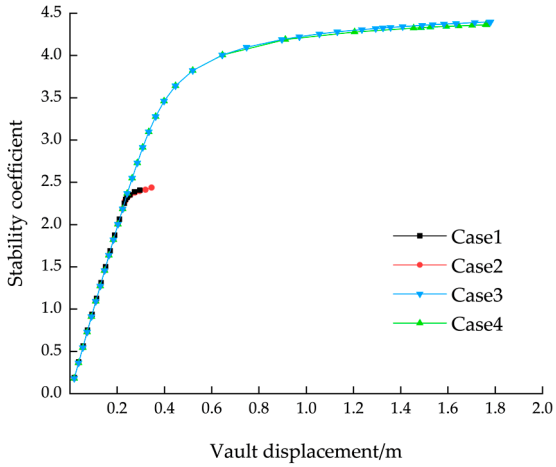

Figure 14. Load–displacement curves for different component materials.

4.5.2. Effects of Different Stiffnesses in Arch Ribs

To study the influence of the stiffness of the arch rib on the stability of the steel truss bridge, the elastic modulus of the arch rib was taken as 0.50E, 0.75E, 1.00E, 1.25E, 1.50E, 1.75E, and 2.00E. Without modifying the density and cross section of the arch ribs, the calculations are shown in Table 12 and Figure 15.

Table 12. Stability eigenvalue of the first ten orders for different multiple of stiffness in arch ribs.

Stiffness (×E)	Stability Eigenvalue									
	1	**2**	**3**	**4**	**5**	**6**	**7**	**8**	**9**	**10**
0.50	3.271	9.217	12.526	13.114	14.609	15.592	15.873	17.247	18.321	20.141
0.75	4.698	12.272	16.837	16.958	20.109	22.021	22.129	23.817	26.029	28.211
1.00	6.196	15.734	20.927	21.735	25.909	28.681	29.088	30.515	34.683	36.219
1.25	7.372	18.184	23.19	25.083	29.635	33.195	34.067	35.681	40.393	43.336
1.50	8.64	21.089	25.981	28.989	33.802	38.455	39.555	41.159	47.109	50.466
1.75	9.87	23.972	28.608	32.811	37.657	43.586	44.768	46.416	53.537	57.355
2.00	11.068	26.835	31.103	36.563	41.247	48.626	49.736	51.495	59.694	64.033

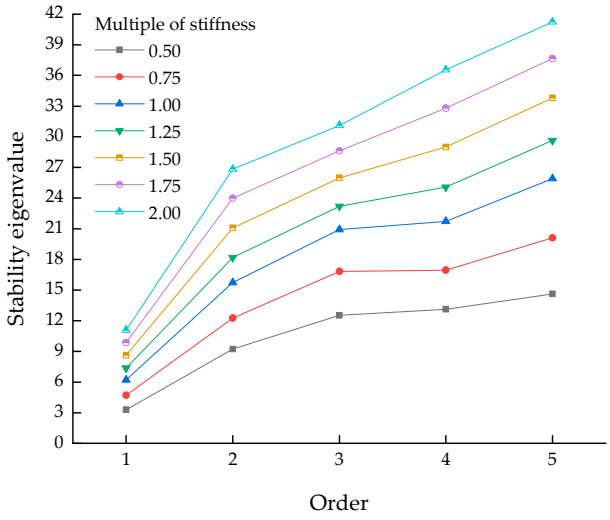

Figure 15. Effects of different stiffnesses of the arch rib on the stability eigenvalue.

The stability eigenvalue of the steel truss arch bridge increased significantly when the arch rib stiffness increased in the range of 0.5E to 1.0E, with the absolute value of variation of first-order buckling being 55.63% and 36.27% relative to the original design. As the arch rib stiffness increased in the range of 1E to 2E, the stability eigenvalue of the steel truss arch bridge increased relatively slowly, with growth ratios of 14.68%, 25.31%, and 33.40% for first-order buckling. It can be concluded that the stability of the structure increases when the stiffness of the arch ribs increases within a certain range, but it is not directly proportional to the variation of the stiffness of the arch rib.

4.5.3. Effects of Different Stiffnesses in Struts

Wind struts are an essential member to connect two pieces of truss arch ribs, change the stiffness of a wind strut in the same way as arch rib stiffness, and analyze the effect of wind struts' stiffness changes on the stability of a steel truss arch bridge. Without modifying the density and cross section of the wind struts, the calculations are shown in Table 13 and Figure 16.

Table 13. Stability eigenvalue of the first ten orders for different multiple of stiffness in structs.

Stiffness (×E)	Stability Eigenvalue of First Ten Orders									
	1	**2**	**3**	**4**	**5**	**6**	**7**	**8**	**9**	**10**
0.50	5.663	13.442	18.298	18.613	21.356	25.021	25.783	27.677	30.198	32.093
0.75	5.902	14.379	19.505	19.817	23.614	27.014	27.708	28.175	32.144	34.345
1.00	6.196	15.734	20.927	21.735	25.909	28.681	29.088	30.515	34.683	36.219
1.25	6.179	16.076	20.740	22.178	26.167	27.777	29.177	31.327	34.287	37.190
1.50	6.274	16.870	21.212	23.190	26.996	27.807	29.892	32.505	35.029	38.272
1.75	6.353	17.636	21.628	24.132	27.640	27.867	30.489	33.533	35.664	39.244
2.00	6.422	18.378	22.003	25.020	27.818	28.289	31.008	34.455	36.228	40.143

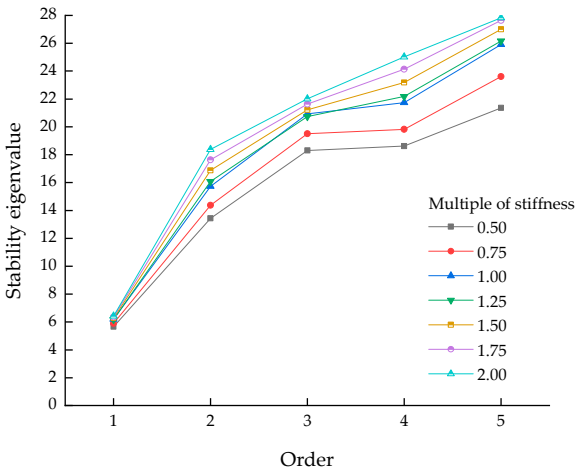

Figure 16. Effects of different stiffnesses in the struts on the stability eigenvalue.

The stability eigenvalue of the steel truss arch bridge increased slightly when the struts stiffness increased in the range of 0.5E to 2.0E, with the absolute value of the variation of first-order buckling of 8.35%, 4.48%, 0.28%, 1.51%, 2.74%, and 3.78% relative to the original design. Higher-order buckling eigenvalues were also not significant. It can be concluded that the change amplitude of the stability of the structure is not significant when the stiffness of the wind struts increases within a certain range.

4.6. Struts

4.6.1. Stability of Different Types of Struts

Stability analyses indicated that the bridge has poor out-plane stability. The first four instability modes of the arch bridge are all out-plane instabilities, with the first-order flexural mode of the asymmetric arch bridge being a lateral buckle in the local chords near the foot of the short half-arch. The third-order buckling mode is out-plane instability of the chords in the region where the long half-arch meets the bridge deck, while the second- and fourth-order are the whole arch ribs lateral buckle. The in-plane instability of this bridge occurs in the sixth order. The out-plane buckling eigenvalue is much smaller than the lowest-order in-plane stability coefficients for all the cases in Table 7. Accordingly, based on the original design of the bridge, the structural form of the cross and diagonal struts was modified, as shown in Figure 17, to investigate the impact of the wind bracing form on the stability of the structure.

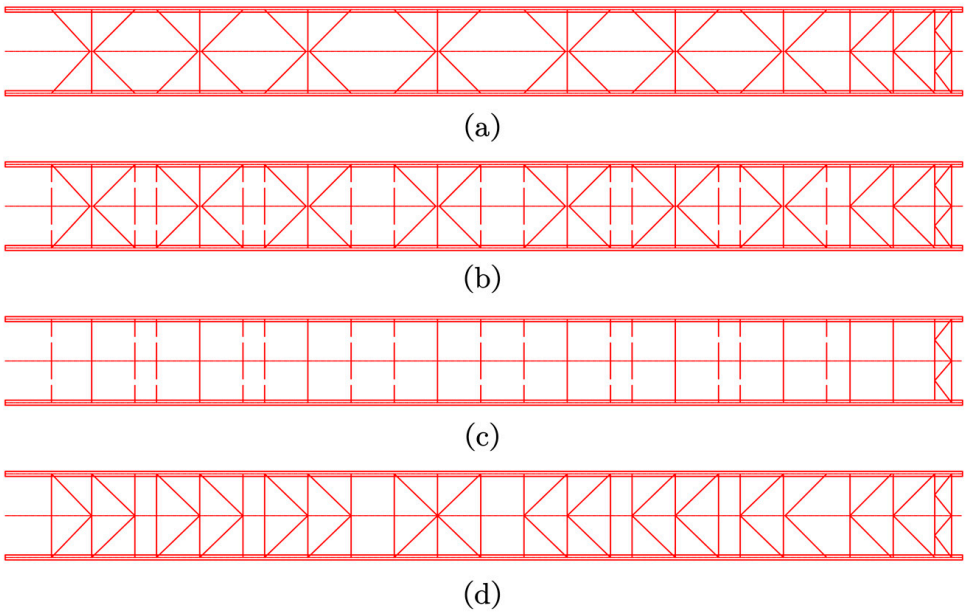

Figure 17. Different schemes of struts: (**a**) original scheme; (**b**) adding more cross struts; (**c**) only cross struts; and (**d**) substitution with k-shape struts.

a. Original design: double cross struts with partial K-shaped struts;
b. Doubled cross bracing at the upper and lower chords based on Scheme a;
c. Removed upper and lower chord diagonal struts based on Scheme b;
d. Replaced double cross struts with K-shaped braces based on Scheme b.

Cross bracing has an important effect on the stability of two-piece truss arch structures, and it is worth discussing the ability of its quantity to enhance the stability of the structure. The impact of the change in the number of cross braces can be determined by comparing the overall stability of the bridges in schemes a and b. As can be seen from Table 14, except for a small decrease in the first-order stabilization coefficients, the remaining four orders improved to a certain extent, with the percentage of improvement ranging from 20% to 30%. The enhancement of the fourth-order stability of the arch bridge is the most obvious, the in-plane instability mode is improved from the sixth order to the fourth order, and the fourth buckling shape of Scheme b is shown in Figure 18b.

Table 14. Stability eigenvalue of different strut schemes.

Order No.	Strut Schemes							
	(a)		(b)		(c)		(d)	
	Eigenvalue	Buckling Mode	Eigenvalue	Buckling Mode	Eigenvalue	Buckling Mode	Eigenvalue	Buckling Mode
1	6.061	Out-plane	5.943	Out-plane	2.324	Out-plane	6.097	Out-plane
2	15.249		19.561		3.531		19.704	
3	20.187		24.154		3.770		24.490	
4	21.069		27.271	In-plane	5.216		26.656	In-plane
5	25.095		28.594		6.642		28.692	

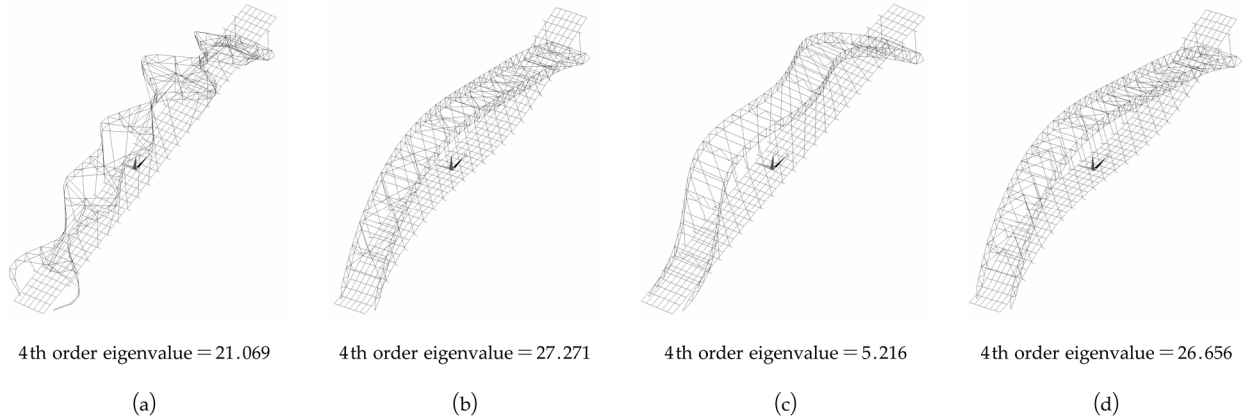

Figure 18. The fourth buckling shape for the bridge with different types of struts: (**a**) Scheme a, (**b**) Scheme b, (**c**) Scheme c, and (**d**) Scheme d.

Scheme b and scheme c were compared to analyze the effect of diagonal bracing on the stability of arch bridges. After removing all the diagonal braces on the arch bridge, the overall stability was significantly lower than that in the case with diagonal braces, the first-order stability coefficients did not comply with the requirements of the current specification, and the average reduction in the stability ratio of the first five orders was 77%. Through the buckling eigenvalue and fourth instability shape shown in Figure 18c, it was recognized that the diagonal bracing has a great influence on the stability of the arch ribs, and the cross bracing cannot satisfy the lateral stability requirements of the steel truss arch bridge.

Scheme d changed the double cross struts except for the arch top in scheme b to K-shaped diagonal bracing, and the low-order stability of the arch bridge was almost unchanged. Meanwhile, its buckling mode was basically the same as scheme b, as shown in Figure 18. Therefore, the function of K-shaped wind braces in steel truss arch bridges is consistent with that of double cross struts, which can be selected according to the difficulty of on-site construction and the degree of industrialization of the manufacture via members.

4.6.2. Stability for Adding Bracing in Certain Locations

To ensure that the bridge is accessible to traffic, the height of the cross bracing in the area where the bridge deck intersects with the short half-arch should not be set too low so that the out-plane calculated length of the chord in the foot section of the short half-arch is longer. The first-order buckling modes of the arch bridge under all working conditions resulted in instability in the short half-arches out of the plane. Similarly, for the region where the bridge deck intersects with the long half-arch, there was a typical instability condition, which mostly occurred in the second- or third-order flexural modes. Therefore, four other new types of schemes were designed to study the effects of cross bracing in certain locations, as shown in Figure 19.

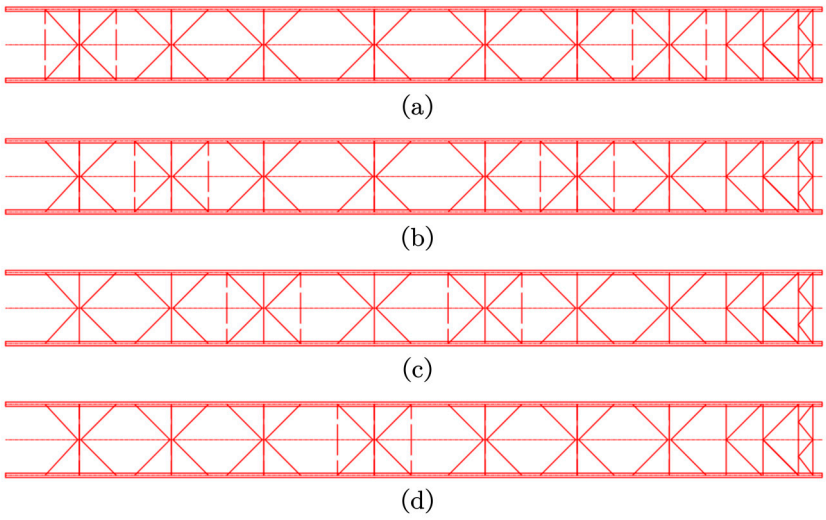

Figure 19. Cross bracing added in different locations: (**a**) Case 1, (**b**) Case 2, (**c**) Case 3, and (**d**) Case 4.

According to Figure 20, after adding the cross bracing in a certain location, the bridge's out-of-plane stability improved by various degrees. The average eigenvalue of the first five lowest orders increases was 18.10%, 18.73%, 14.39%, and 6.16% for Case 1 to Case 4, respectively. Comprehensively comparing the four cases revealed that Case 3 and Case 4 achieved little improvement in arch rib stability. And the closer the reinforcement location to the mid-structs, the worse the reinforcement efficiency.

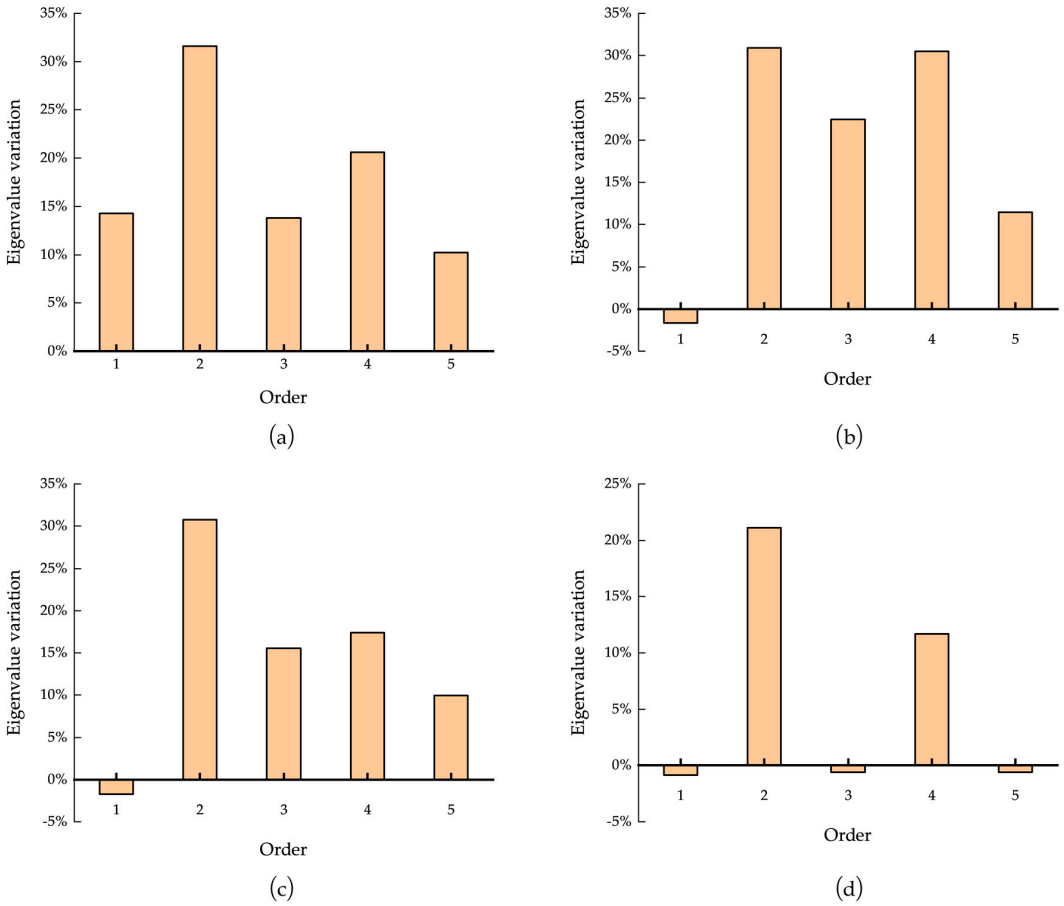

Figure 20. Eigenvalues' increasing rate after adding cross bracing: (**a**) Case 1, (**b**) Case 2, (**c**) Case 3, and (**d**) Case 4.

Although the discrepancy between Case 1 and Case 2 was not significant in average value, Case 1 achieved a more significant improvement in the first-order stability of the bridge, which was more in compliance with the design principle of reinforcing the lowest-order buckling mode of the bridge. Therefore, it is recommended that more cross bracing be added at the intersection of the arch ribs and the deck.

4.7. Effects of Temperature

4.7.1. Effects of Temperature under Construction

The diurnal variation of the mountain ravine was relatively great, and the construction period of the large-span bridge was long, so it was difficult to keep the temperature of each segment of the arch rib the same during installation. The standard temperature of this bridge was set to 20 °C, according to the field environment. The displacement changes of each control point of the arch rib in the horizontal and vertical directions were analyzed in the maximum cantilever state under the conditions of temperature rises of 30, 20, and 10 °C and temperature drops of 30, 20, and 10 °C, respectively. The displacement of control points in different temperatures is shown in Tables 15 and 16.

Table 15. Horizontal displacement of control points under different temperatures.

Control Point	Horizontal Coordinate (m)	Horizontal Displacement Variation (cm)					
		Temperature Rises by 30 °C	Temperature Rises by 20 °C	Temperature Rises by 10 °C	Temperature Drops by 10 °C	Temperature Drops by 20 °C	Temperature Drops by 30 °C
YG 1	15	0.88	0.59	0.29	−0.29	−0.59	−0.88
YG 2	28	1.99	1.32	0.66	−0.66	−1.32	−1.99
YG 3	42	3.17	2.11	1.06	−1.06	−2.11	−3.17
YG 4	56	4.28	2.86	1.43	−1.43	−2.86	−4.28
YG 5	70	5.31	3.54	1.77	−1.77	−3.54	−5.31
YG 6	84	6.25	4.17	2.08	−2.08	−4.17	−6.25
YG 7	98	7.09	4.73	2.36	−2.36	−4.73	−7.09
YG 8	112	7.83	5.22	2.61	−2.61	−5.22	−7.83
YG 9	126	8.48	5.65	2.83	−2.83	−5.65	−8.48
YG 10	140	9.03	6.02	3.01	−3.01	−6.02	−9.03
LG 12	147	−9.23	−6.15	−3.08	3.08	6.15	9.23
LG 11	154	−8.96	−5.97	−2.99	2.99	5.97	8.96
LG 10	168	−8.39	−5.59	−2.80	2.80	5.59	8.39
LG 9	182	−7.77	−5.18	−2.59	2.59	5.18	7.77
LG 8	196	−7.10	−4.74	−2.37	2.37	4.74	7.10
LG 7	210	−6.39	−4.26	−2.13	2.13	4.26	6.39
LG 6	224	−5.63	−3.75	−1.88	1.88	3.75	5.63
LG 5	238	−4.81	−3.20	−1.60	1.60	3.20	4.81
LG 4	252	−3.93	−2.62	−1.31	1.31	2.62	3.93
LG 3	266	−2.98	−1.99	−1.00	1.00	1.99	2.98
LG 2	280	−1.98	−1.32	−0.66	0.66	1.32	1.98
LG 1	294	−0.91	−0.61	−0.30	0.30	0.61	0.91

The curves shown in Figure 21 demonstrate that the rising and dropping of temperatures affect the horizontal and vertical displacements of the structure. The displacement variation was approximately linear, with the values of the displacements at the control points changing multiplicatively at different temperatures and within 0.02 cm. When the temperature rises, the buckling anchors elongate due to the material's own thermal expansion and contraction properties. The vertical elevation of the arch rib control point decreases, and the horizontal displacement elongates towards the center of the river. When the temperature drops down, the structural deformation is the opposite, and the arch rib and buckling cable deformation are coupled with each other.

Table 16. Vertical displacement of control points under different temperatures.

Control Point	Horizontal Coordinate (m)	Vertical Displacement Variation (cm)					
		Temperature Rises by 30 °C	Temperature Rises by 20 °C	Temperature Rises by 10 °C	Temperature Drops by 10 °C	Temperature Drops by 20 °C	Temperature Drops by 30 °C
YG 1	15	0.24	0.16	0.08	−0.08	−0.16	−0.24
YG 2	28	−0.27	−0.18	−0.09	0.09	0.18	0.27
YG 3	42	−1.02	−0.68	−0.34	0.34	0.68	1.02
YG 4	56	−1.90	−1.27	−0.63	0.63	1.27	1.90
YG 5	70	−2.89	−1.92	−0.96	0.96	1.92	2.89
YG 6	84	−3.94	−2.63	−1.31	1.31	2.63	3.94
YG 7	98	−5.05	−3.37	−1.68	1.68	3.37	5.05
YG 8	112	−6.21	−4.14	−2.07	2.07	4.14	6.21
YG 9	126	−7.41	−4.94	−2.47	2.47	4.94	7.41
YG 10	140	−8.64	−5.76	−2.88	2.88	5.76	8.64
LG 12	147	−3.61	−2.41	−1.21	1.21	2.41	3.61
LG 11	154	−3.33	−2.22	−1.11	1.11	2.22	3.33
LG 10	168	−2.77	−1.85	−0.93	0.93	1.85	2.77
LG 9	182	−2.26	−1.51	−0.75	0.75	1.51	2.26
LG 8	196	−1.78	−1.19	−0.59	0.59	1.19	1.78
LG 7	210	−1.34	−0.90	−0.45	0.45	0.90	1.34
LG 6	224	−0.94	−0.63	−0.31	0.31	0.63	0.94
LG 5	238	−0.58	−0.39	−0.19	0.19	0.39	0.58
LG 4	252	−0.25	−0.17	−0.09	0.09	0.17	0.25
LG 3	266	0.02	0.02	0.01	−0.01	−0.02	−0.02
LG 2	280	0.25	0.17	0.08	−0.08	−0.17	−0.25
LG 1	294	0.40	0.27	0.13	−0.13	−0.27	−0.40

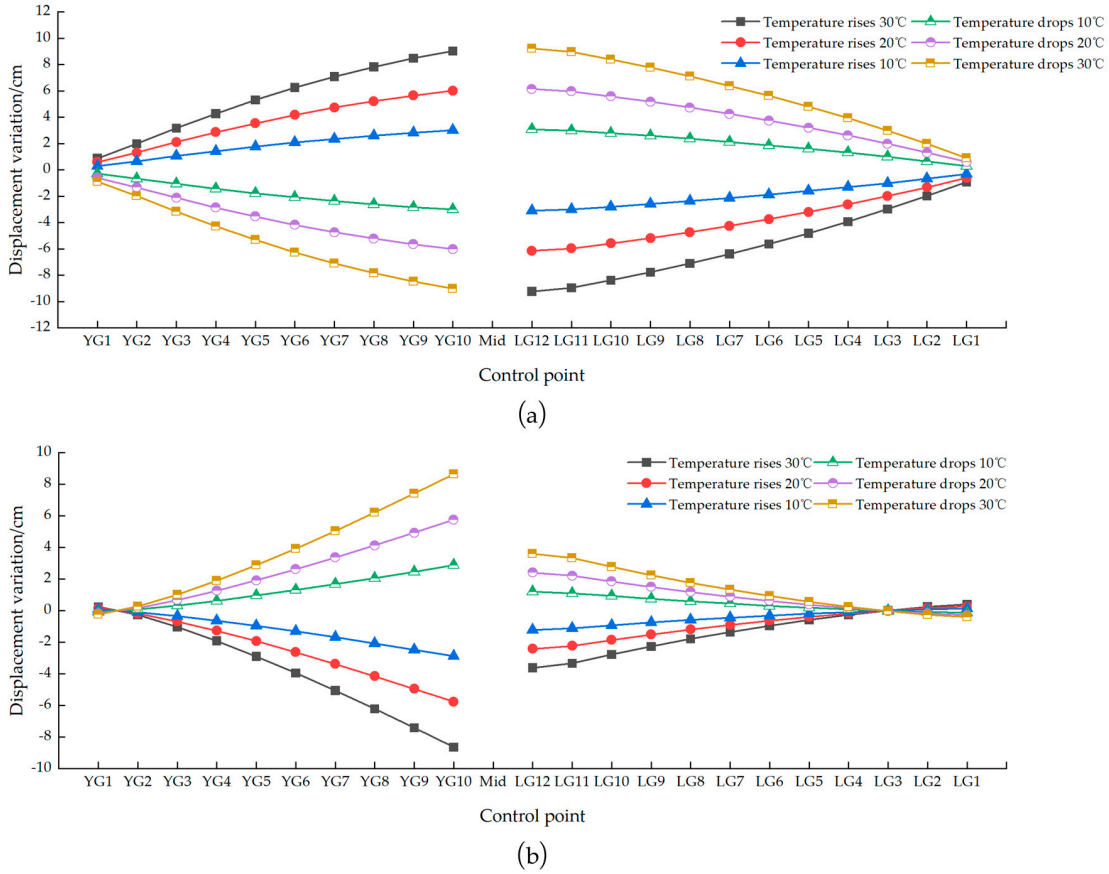

Figure 21. Displacement of control points under different temperatures: (**a**) horizontal displacement and (**b**) vertical displacement.

Considering the temperature correction of the installation profile during construction, the modified expression is defined in Equation (3):

$$H = H_0 + \Delta y \tag{3}$$

Δy is the corrected value for the effect of temperature on the structure during the current construction stage. Equation (3) approximates the effect of temperature on the structure as a linear relationship, which has some error in theory. However, an appropriate pre-lift increase can eliminate or reduce the lowering of the elevation caused by the rusting of the anchor cable and the relaxation of the clip sheet at the anchorage point.

4.7.2. Effects of Temperature under Operation

The conditions for temperature effects during the operation stage of the bridge are the same as in the construction stage. The stability performance of the bridge under geometric nonlinearity was calculated, and the curves for the stability coefficient and vault displacement are shown in Figure 22.

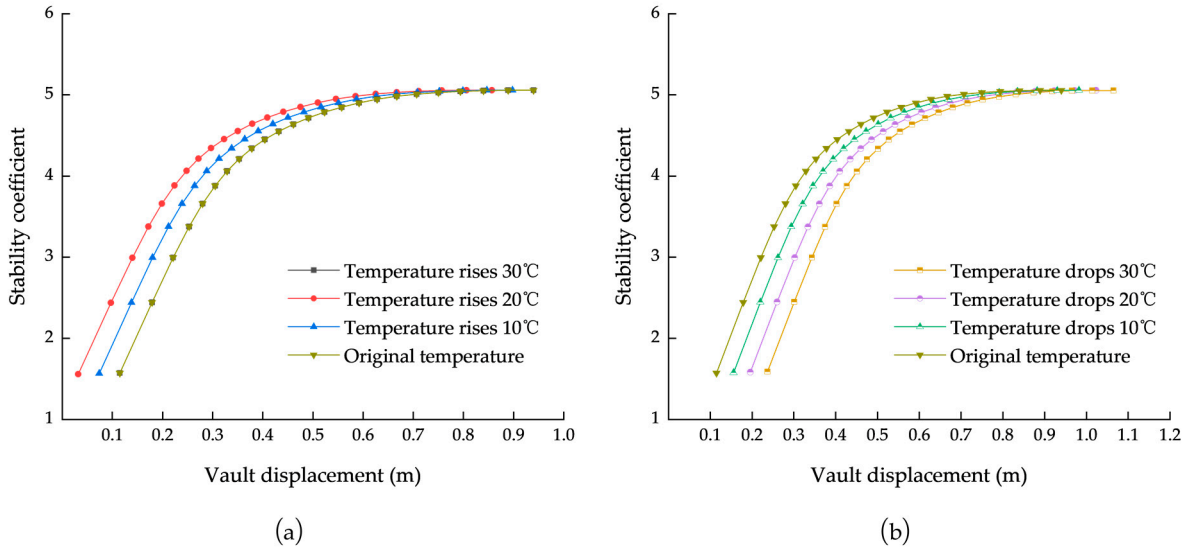

Figure 22. Load–displacement curves for different temperatures: (**a**) displacement in condition of temperature rise; (**b**) displacement in condition of temperature drop.

Under the temperature-rise condition, the load–displacement curves of the bridge were offset to the left. The structure would reach the plastic state earlier, and the capacity of displacement was smaller compared to the original condition. In the temperature-drop condition, the load–displacement curves of the bridge were offset to the right. The structure moved into the plastic state later, and the displacement was greater than that of the original condition by 4.47%, 8.83%, and 13.30%, while the ultimate load was constant. The greater the temperature reduction, the more noticeable its strengthening effect. Overall, the stability of asymmetric steel truss arch bridges can be slightly improved when cooling down and decreased when warming up, but the effect is small.

5. Conclusions

The Loushui River Bridge adopts a double-hinged arch structure system with high and low arches, avoiding the risk of large-scale excavation in mountainous areas. The arch consists of a lateral two-piece N-shaped structure with simple wind struts, while the arch axis features a virtual catenary line, which is a novel structure.

The segmental suspension installation method based on CHS is used for the construction of the Loushui River Bridge, which improves the construction speed and ensures the safety of structural system transformation during the process. The difficult problem of

transportation in mountainous areas has been overcome, and the limited construction site has been greatly utilized to minimize the damage to the environment.

A case study on the stability of the Loushui River Bridge through construction and operation was conducted by taking into account the complex construction conditions and steep terrain. A series of related three-dimensional finite element models were developed and validated numerically and experimentally. The stability eigenvalue and load–displacement curves were calculated. The results were as follows:

- The stability of the asymmetric structure meets the design requirements in both the construction and operation stages. However, according to the buckling analysis, the dominant instability shape is out of plane, and in-plane buckling only occurs in a high order, which reflects that the bridge is most affected by lateral wind during either the construction or operation stages. Due to the influence of deep valley topography, mountain bridges should emphasize wind resistance.
- The arch rib before closure is a cantilever system, and the wind hazard in the ravine area has the greatest influence on the construction of the bridge. Compared with the windless condition, the stability of the bridge under a wind load is reduced by nearly 50%. The application of wind cables and temporary wind braces in every segment can resist the wind load well, which controls the lateral deformation of the arch rib within 5 cm.
- The geometric imperfections have a slight influence on the linear analysis of the structure, while the stability analysis when considering nonlinearity is significantly affected by imperfections. The pattern of variation shows that the bridge's stability decreases with an increase in geometric imperfections.
- The asymmetry of the steel truss arch ribs has a significant impact on the overall stability of the bridge. Asymmetry greatly reduces the deformation tolerance of arch bridges, causing premature failure of the structures.
- The performance of steel arch ribs determines the stability of the entire arch bridge. Changes in the stiffness of the arch ribs have a greater effect on the stability, while changes in the stiffness of the wind braces have an average effect. The wind resistance of diagonal bracing is greater than that of simple transverse bracing, which can significantly improve the mechanical properties of the bridge. The weak point of the Loushui River Bridge is located at the intersection of the arch ribs and the bridge deck, where the addition of wind bracing is an effective way to improve the lateral stability and stiffness of the bridge.
- Temperature has a certain influence on the construction of arch ribs. The temperature load influence should be considered during construction, and the installation elevation of the arch rib structure should be corrected to minimize error. The effect of temperature on the stability of asymmetric steel truss arch bridges during the operational phase is not significant, and the overall stability is good, based on the environment of the Loushui River Bridge.

This paper has analyzed the Loushui River Bridge's aspects of design and construction. For this kind of bridge, the following aspects are worthy of further study. The Loushui River Bridge adopts a unified arch axis. How to design the ratio of an arch axis on both sides of the arch to adapt to the terrain with greater elevation differences that may be encountered in the future is worth studying. It is assumed that the cable tower only transmits vertical force to the fastening tower during the hoisting of the arch segment. However, the vertical force concerning the center of the fastening tower section is eccentric, and the resulting change in the alignment of the arch rib installation is worthy of study.

Author Contributions: Conceptualization, Y.T.; Methodology, Y.T.; Software, Y.T.; Investigation, Y.T.; Resources, P.L., J.T. and Y.Z.; Writing—original draft, Y.T.; Writing—review & editing, J.S.; Visualization, J.S.; Supervision, J.S.; Project administration, P.L. and J.T. All authors have read and agreed to the published version of the manuscript.

Funding: This research was funded by The Open Key Fund Sponsored Program of State Key Laboratory for Bridge Health and Safety (No. BHSKL19-06-KF).

Data Availability Statement: Data are contained within the article.

Conflicts of Interest: Peng Liu was employed by the company Hubei Gaolu Highway Engineering Supervision & Consultation Co., Ltd, Jun Tao was employed by the company China Railway Major Bridge Engineering Group No. 6 Engineering Co., Ltd., Yueyue Zhao was employed by the company China Railway Siyuan Survey and Design Group Co., Ltd. The remaining authors declare that the research was conducted in the absence of any commercial or financial relationships that could be construed as a potential conflict of interest.

Nomenclature

E	Elastic modulus
ρ	Weight per unit volume of material
γ	Poisson's ratio
σ_y	Yield stress of material
σ	Stress under load
ε	Total strain
ε_e	Elastic strain of the structure under load
ε_{ns}	No-stress strain
H	Actual elevation of the measuring point
H_0	Ideal elevation of the measuring point
Δy	Correction value of temperature's influence on the structure

References

1. Zhao, W.; Xie, Q. Selection of Positions for Yesan River Bridge Foundations in Yichang-Wanzhou Railway. *J. Southwest Jiaotong Univ.* **2003**, *16*, 57–59.
2. Yan, A.; Xia, Z.; Zhang, J.; Li, Z.; Yin, P. Type Selection for Youshui River Bridge of Zhangjiajie-Jishou-Huaihua Railway in Furong Town. *Bridge Constr.* **2021**, *51*, 112–117.
3. Xu, Y.; Chen, D.; Nie, Z. Erection Techniques for Arch Ring of Long-Span Steel Box Truss Arch Bridge. *World Bridges* **2020**, *48*, 35–39.
4. Wang, R. Key Construction Techniques for Long-Span Railway Arch Bridge in Mountainous Region of Plateau. *Bridge Constr.* **2020**, *50*, 105–110.
5. Jianpeng, S.; Jinbin, L.; Yingbiao, J.; Xiaogang, M.; Zihan, T.; Zhufu, G. Key Construction Technology and Monitoring of Long-Span Steel Box Tied Arch Bridge. *Int. J. Steel Struct.* **2023**, *23*, 191–207. [CrossRef]
6. Liu, Z. Arch Rib Erection Techniques of Long-Span Asymmetric Arch Bridge in Mountainous Area. *World Bridges* **2023**, *51*, 39–46. [CrossRef]
7. Wang, Y. Construction Techniques for Erection of Arch Rib of Main Bridge of Guizhou Yachi River Bridge on Chengdu-Guiyang Railway. *Bridge Constr.* **2017**, *47*, 104–108.
8. Fang, N.; Xu, X.; Wang, S. Design of Heavy Cable Crane for Zigui Changjiang River Highway Bridge. *Bridge Constr.* **2022**, *52*, 116–123.
9. Hui-Jun, L.; Zeng-Li, P.; Chun-Liang, Y.; Yue-Ming, T. Application of Advanced Reliability Algorithms in Truss Structures. *Int. J. Space Struct.* **2014**, *29*, 61–70. [CrossRef]
10. Bonopera, M.; Chang, K.-C.; Chen, C.-C.; Lin, T.-K.; Tullini, N. Bending tests for the structural safety assessment of space truss members. *Int. J. Space Struct.* **2018**, *33*, 138–149. [CrossRef]
11. Maes, K.; Peeters, J.; Reynders, E.; Lombaert, G.; De Roeck, G. Identification of axial forces in beam members by local vibration measurements. *J. Sound Vib.* **2013**, *332*, 5417–5432. [CrossRef]
12. Wang, Y.; Ibarra, L.; Pantelides, C. Seismic Retrofit of a Three-Span RC Bridge with Buckling-Restrained Braces. *J. Bridge Eng.* **2016**, *21*, 04016073. [CrossRef]
13. Celik, O.C.; Bruneau, M. Seismic behavior of bidirectional-resistant ductile end diaphragms with buckling restrained braces in straight steel bridges. *Eng. Struct.* **2009**, *31*, 380–393. [CrossRef]
14. Wang, J.; Ma, P. Mechanical performance analysis of long-span steel truss arch bridge during construction process. *Highw. Eng.* **2022**, *67*, 204–209.
15. Chai, S.B.; Yang, Q.H.; Wang, X.L.; Yu, Y.L.; Zhuang, H.F. Stability Analysis of Long-span Half-through Steel Box Tied Arch Bridge during Construction. *Sci. Technol. Eng.* **2022**, *22*, 8095–8102.
16. Tong, X.L.; Fang, Z. Study on Stability Safety Factor of Bridge Structure Based upon Reliability Index. *J. China Railw. Soc.* **2014**, *36*, 102–108.

17. Dou, C.; Jiang, Z.Q.; Pi, Y.L.; Gao, W. Elastic buckling of steel arches with discrete lateral braces. *Eng. Struct.* **2018**, *156*, 12–20. [CrossRef]
18. Zhao, M.; Chen, S.T.; Sun, Z.X.; Xu, H.W.; Huang, X.M. Study on Stability of New Long-span Railway Emergency Steel Truss Girder. *J. China Railw. Soc.* **2022**, *44*, 119–127.
19. Sun, X.P.; Zheng, B.; Hu, J. Analysis Method of the Second Order Aerostatic Stability for Long-span Steel Truss Arch Bridge. *Highw. Eng.* **2017**, *42*, 337–342.
20. Lyu, L.; Zhong, H.; Gu, Y.; Ren, W.; Zhao, L. Main Arch Ring Nonlinear Stability Assessment of Nanpan River Super Large Bridge on Yunnan-Guangxi Railway. *Railw. Eng.* **2019**, *59*, 27–31.
21. Bouras, Y.; Vrcelj, Z. Non-linear in-plane buckling of shallow concrete arches subjected to combined mechanical and thermal loading. *Eng. Struct.* **2017**, *152*, 413–423. [CrossRef]
22. Yan, Q.; Luo, N.; Han, D.; Wang, W. Nonlinearity and Stability Analysis for A Long-Span Arch Bridge. *J. South China Univ. Technol.* **2000**, *13*, 64–68.
23. Han, X.; Zhu, B.; Zhang, L.; Zhu, J.B.; Xiang, B.S. Dual Non-Linear Stability Research on Long-Span Concrete-Filled Steel Tubular Arch Bridge. *J. Chongqing Jiaotong Univ.* **2013**, *32*, 856–859.
24. Shi, Z.; Zhang, Y.; Zhang, Y.Z.; Xia, Z.C. Study on Stability of Long-Span Railway Through Bridge with Steel Truss Girder and Flexible Arch. *China Railw. Sci.* **2019**, *40*, 52–58.
25. Chen, J.; Hu, W.J. Study on Overall Stability of Long-span Deck Concrete-filled Steel Tubular Arch Bridge. *Railw. Eng.* **2020**, *60*, 16–19.
26. Zhang, J.Q.; Ji, R.C. Elastic Stability Analysis of Railway Long Span CFST Arch Bridge. *Railw. Eng.* **2020**, *60*, 12–15.
27. Kong, D.D.; Yu, X.K.; Hao, X.W.; Yu, Y.; Gu, Z.F. Influence of Local Instability of Members on Overall Stability of Steel Truss Arch Bridge. *J. Northeast For. Univ.* **2021**, *49*, 116–121. [CrossRef]
28. Wei, Y.; Jin, Z. Research on Wind Resistance of Stiff-Skeleton Arch Ring of Long-Span Concrete-Filled Steel Tubular Arch Bridge During Vertical Rotation Construction. *Bridge Constr.* **2023**, *53*, 75–81. [CrossRef]
29. Su, Y.-H.; Wu, Y.-R.; Sun, Q. Wind-Induced Response Analysis for a Fatigue-Prone Asymmetric Steel Arch Bridge with Inclined Arch Ribs. *Adv. Mater. Sci. Eng.* **2022**, *2022*, 3489390. [CrossRef]
30. Li, X.; Yan, M.; Luo, P.; Yu, Q. Study on Mechanical Characteristics of Asymmetric Curved Arch Bridge with Outward-Inclined Ribs. *Railw. Stand. Des.* **2014**, *58*, 81–84. [CrossRef]
31. Hu, X.K.; Xie, X.; Tang, Z.Z.; Shen, Y.G.; Wu, P.; Song, L.F. Case study on stability performance of asymmetric steel arch bridge with inclined arch ribs. *Steel Compos. Struct.* **2015**, *18*, 273–288. [CrossRef]
32. Hu, X.; Huang, Y.; Wang, D.; Liu, A. Numerical simulation study of a long-span asymmetric bowstring arch bridge. *Highway* **2021**, *66*, 208–213.
33. Sun, J.; Xie, J.; Liu, C. Investigating asymmetric spatial butterfly-shaped steel arch bridges: A case study. *Proc. Inst. Civ. Eng.-Bridge Eng.* **2021**, *174*, 13–27. [CrossRef]
34. Peng, G.; Gao, W.; Wu, Q. Parameter analysis on the stability of butterfly shape arch bridge. *J. Fuzhou Univ.* **2017**, *45*, 512–516.
35. Cheng, X.X.; Dong, J.; Cao, S.S.; Han, X.L.; Miao, C.Q. Static and Dynamic Structural Performances of a Special-Shaped Concrete-Filled Steel Tubular Arch Bridge in Extreme Events Using a Validated Computational Model. *Arab. J. Sci. Eng.* **2018**, *43*, 1839–1863. [CrossRef]
36. Ma, M.; Qian, Y.; Xu, B. Analysis of Ultimate Load-Carrying Capacity of Crescent-Shaped Concrete-Filled Steel Tube Arch Bridge. *J. Southwest Jiaotong Univ.* **2017**, *52*, 678–684+714.
37. Li, S.Y.; Kohlmeyer, C.; Muller, F. Global Stability Analysis of an Asymmetrical Long-Span Concrete-Filled Steel Tube Arch Bridge. In Proceedings of the ARCH'10—6th International Conference on Arch Bridges, Fuzhou, China, 11–13 October 2010; p. 7.
38. Gou, H.; He, Y.; Zhou, W.; Bao, Y.; Chen, G. Experimental and numerical investigations of the dynamic responses of an asymmetrical arch railway bridge. *Proc. Inst. Mech. Eng. Part F J. Rail Rapid Transit* **2018**, *232*, 2309–2323. [CrossRef]
39. Liu, X.H.; Ding, D.H.; Feng, P.C. Key Design Techniques of Long-Span Two-Hinge Steel Truss Arch Bridge with High and Low Arch Seats. *Bridge Constr.* **2022**, *52*, 101–108.
40. *GB 50017-2003*; Code for Design of Steel Structures. Standardization Administration of China: Beijing, China, 2003.
41. *JTG D60-2004*; General Code for Design of Highway Bridges and Culverts. CCCC First Highway Construction Co., Ltd.: Beijing, China, 2004.
42. *GB/T 714-2015*; Structural Steel for Bridge. Standardization Administration of China: Beijing, China, 2015.
43. Ge, J.Y. *Guide for Use of Midas Civil Bridge Engineering Software*; People's Communications Press: Beijing, China, 2013.
44. *JTG/T D60-01-2004*; Wind-Resistant Design Specification for Highway Bridges. CCCC First Highway Construction Co., Ltd.: Beijing, China, 2004.
45. ANSYS. *Structural Finite Element Analysis (FEA) Software*; ANSYS Inc.: Canonsburg, PA, USA, 2022.